Front. Chem. Sci. Eng. 2025, 19(9): 77
https://doi.org/10.1007/s11705-025-2586-6

RESEARCH ARTICLE

Boosting visible-light photocatalytic performance of exfoliated carbon nitride nanosheets via optimizing dopant decoration for efficient pollutant removal

Kingsley Igenepo John, Touma B. Issa, Goen Ho, Aleksandar N. Nikoloski, Dan Li (✉)

Harry Butler Institute, College of Science, Technology, Engineering & Mathematics, Murdoch University, Murdoch WA 6150, Australia

Abstract This study systematically studied the effects of Pr, Fe, and Na as representative rare earth, transition, and alkali metal dopants, respectively, on the photocatalytic activity of exfoliated graphitic carbon nitride (g-C_3N_4). The doped exfoliated g-C_3N_4 samples were prepared by integrating precursor ion intercalation into the pre-formed g-C_3N_4 with thermal treatment. The as-prepared catalysts were examined for crystal, textural, chemical, optical, and photoelectrochemical properties to explore the correlation between dopants and photocatalytic activity of the resulting composites. The detailed analyses revealed that the Pr-doped g-C_3N_4 exhibited superior photocatalytic activity in degrading methylene blue under visible light, achieving a ~96% removal in 40 min. This was not only better than the activity of g-C_3N_4, but also much higher than that of Na-doped g-C_3N_4 or Fe-doped g-C_3N_4. The kinetic rate constant using Pr-doped g-C_3N_4 was 3.2, 5.1, and 2.0 times greater than that of the g-C_3N_4, Fe-doped g-C_3N_4, and Na-doped g-C_3N_4, respectively. The enhanced performance was attributed to its inherent characteristics after optimal tuning, including good surface area, improved porosity, enhanced visible light absorption, suitable electronic band structure, increased charge carrier density, promoted charge separation, and reduced charge transfer resistance. In addition, the optimized Pr(0.4)g-C_3N_4 was used to study the photocatalytic removal of methylene blue in detail under conditions with different initial methylene blue concentrations, types of dyes, catalyst dosages, initial solution pH, counter ions, and water matrices. Our results demonstrated the high photocatalytic activity of Pr(0.4)g-C_3N_4 under varying conditions, including in real wastewater media, which were collected from our local municipal wastewater treatment plant. The observed good reusability and stability after five cycles of photocatalytic degradation test further suggested a promising potential of Pr(0.4)g-C_3N_4 for practical application in wastewater treatment.

Keywords graphitic carbon nitride, alkaline metal, transition metal, rare earth, exfoliation, photocatalysis, pollutant removal

1 Introduction

Graphitic carbon nitride (g-C_3N_4) is a non-metallic organic semiconductor, which has been extensively researched as a photocatalyst in various applications, such as hydrogen production, sensing, methanation, and environmental remediation. It is well known for its advantageous properties, including eco-friendliness, facile synthesis, visible light absorption, low cost, and chemical stability. However, the application of bulk g-C_3N_4 has been hampered due to its limited surface area, high recombination of charge carriers, and poor visible light absorption [1]. Consequently, efforts have been devoted to modifying g-C_3N_4 to improve its photocatalytic activity using different strategies [2]. In particular, the metal doping of g-C_3N_4 has been suggested as an effective approach to increase active sites, enlarge surface area, modulate electronic structure, promote optical absorption, and reduce recombination of photogenerated electron-hole pairs. Over the years, there has been ongoing research in exploring different types of metal dopants, including alkali, transition, and rare earth (RE) elements, to boost the photocatalytic activity of resulting g-C_3N_4 composites.

Alkali metals have been well known for several merits, such as no toxicity, low cost, resource abundance, and environmental friendliness [3]. A series of alkali metals have been examined as effective doping additives to modify the photocatalytic activity of g-C_3N_4 [4].

Received March 20, 2025; accepted May 19, 2025; online July 8, 2025

E-mail: l.li@murdoch.edu.au

Experimental work and theoretical calculations suggest that the intercalation of alkali metals into the interlayers or doping of alkali atoms into the conjugated planes of g-C_3N_4 vary electron density, suppress random charge transfer, narrow bandgap, accelerate adsorption, and promote reactant activation [4]. Because of high chemical reactivity, Na^+ has been widely utilized in a range of photocatalytic reactions and thus attempted for modifying the photocatalytic activity of g-C_3N_4 for degradation of rhodamine B (RhB) under visible light [5]. Zhang's group [5] synthesized Na-modified g-C_3N_4, using dicyandiamide monomer and sodium hydrate as precursors, followed by milling and annealing at ~500 °C. The as-prepared catalyst was characterized with a reduced grain size, increased surface area, decreased band gap, and enhanced electron-hole separation when compared to the undoped g-C_3N_4. The optimized Na-modified g-C_3N_4 removed around 48% of RhB (k = 0.0064 min^{-1}) after 120 min of visible-light-initiated reaction, in comparison with ~17% of RhB removal (k = 0.0018 min^{-1}) using the pristine g-C_3N_4. Wu et al. [6] synthesized Na-doped g-C_3N_4 nanotubes using a two-step method, namely hydrothermal reaction of melamine and NaOH as precursors and subsequent microwave irradiation heating. Due to the improved attractive force between layers and the structural defect in the resulting catalyst, it could remove ~90% of RhB in 20 min under visible light and show a 3.2-fold increase in the removal over the pure g-C_3N_4. Especially, the above Na doping into g-C_3N_4 increased surface area relative to the unmodified g-C_3N_4, which is favorable to enhance adsorption and diffusion of target organics and increase active sites available for photocatalytic reaction.

The doping of g-C_3N_4 with transition metals (e.g., Co, Fe, Mn, or Mo) could reduce the band gap of resulting catalysts, due to the hybridization between the d orbitals of transition metals and the p_π orbitals of g-C_3N_4 [7]. In addition, the defects or crystallinity changes which might be introduced after doping can vary the electronic and optical characteristics of g-C_3N_4 [7]. Of the transition metals, iron (Fe) is of particular interest, due to its eco-friendliness, natural abundance, and the merits of Fe^{3+}/Fe^{2+} redox reaction during photocatalysis [8,9]. For instance, Gao et al. [8] fabricated Fe-doped g-C_3N_4 using NH_4Cl as a gas template and $FeCl_3$ as the dopant precursor via a one-step pyrolysis process. The doping with Fe resulted in the extension of visible light absorption, increase of surface area (2.5-fold) and improvement of photocatalytic activity (1.7-fold), over the pure g-C_3N_4. The optimized Fe-decorated g-C_3N_4 removed approximately 75% of methylene blue (MB) after 3 h of visible-light-supported photocatalytic reaction, as compared with around 50% for g-C_3N_4. Microwave radiation (600 W) was applied by Karimi to a mixture of pre-formed g-C_3N_4 (using melamine precursor), Fe_2O_3 nanoparticles, and surfactant sodium dodecyl sulfate [10]. The resulting Fe-doped g-C_3N_4 attained approximately 70% of MB removal within 90 min, as compared to ~15% for the pure g-C_3N_4 under visible light [10]. This was explained by the enhanced electron-hole separation and charge carrier migration during the photocatalysis. However, we noted some intrinsic constraints for the reported Fe-doped g-C_3N_4, such as slow reaction kinetics, low specific surface area, and photo-corrosion, which hindered fast removal of organics and good reusability of catalysts [8,11].

More recently, RE elements have attracted an increasing amount of research interest for use in visible-light-initiated photocatalytic reactions. Their incompletely occupied 4*f* and empty 5*d* orbitals can be used as electron capture centers and increase their optical absorption capability. Some promising results indicated that doping of g-C_3N_4 with RE elements could tune its internal electronic structure and band structure, and in turn result in distinctive photocatalytic activity [12]. Apart from that, improved visible light absorption and enhanced photo-generated charge migration were also observed in the RE-doped of g-C_3N_4, in relative to the parent g-C_3N_4 [12−14]. It should not be neglected that RE ions form complexes with Lewis bases via the interaction between f-orbitals and organic functional groups, which would improve adsorption of organics and then promote photocatalytic reaction [13]. Li et al. [12,13] doped bulk g-C_3N_4 with Sm or Er through one-step thermal polycondensation of $Sm(NO_3)_3{\cdot}5H_2O$ or $Er(NO_3)_3{\cdot}5H_2O$ and melamine at 550 °C. Both the Sm and Er-doped g-C_3N_4 demonstrated much better photocatalytic activity, due to more light harvesting, narrower band gap, and more effective electron-hole separation. Our particular interest in this study in Pr as a dopant is associated with its optical, electrical, and chemical properties, the most stable oxide form of which is Pr_6O_{11} (praseodymium oxide) with +4 and +3 oxidation states [15]. Swetha et al. [16] reported the heterojunction formation between Pr_6O_{11}-containing nanoparticles and g-C_3N_4, assisted by the oxidation state and dynamic cycling of Pr^{3+}/Pr^{4+}, could boost the generation of charge carriers. An early study reported by Shende and coworkers [17] explored the performance upgrade of Pr_6O_{11}/g-C_3N_4, which was prepared by mixing commercial Pr_6O_{11} aggregates and melamine and then annealing at 520 °C, over that of plain g-C_3N_4 for degrading acid violet 7 dye under visible illumination. However, we noted an apparent decrease (10%) in the dye degradation rate of that composite after 4 cycles of use, which could be due to the loss of catalyst (or dopants) during recycling and reuse. Moreover, there was a lack of optimization of the catalyst design and use.

After our literature search, we found there was no systematic study and comparison of the design and properties of g-C_3N_4 with different types of dopants. In the past, limited effort and most of it was concentrated on the comparative results of the doping effect of alkali

metals on the photocatalytic performance of bulk g-C_3N_4 [18,19]. Such a scenario might not be helpful in evaluating each type of elemental dopant in improving the photocatalytic activity of g-C_3N_4. To carry out a systematic comparison and evaluation, g-C_3N_4 catalysts decorated with various types of dopants need to be synthesized under similar conditions, and their photocatalytic performances must be compared under identical conditions. To the best of our knowledge, there has not been a study to investigate the impact of metal dopants from different groups on the photocatalytic performance upgrade of g-C_3N_4, particularly regarding the three major groups of alkali, transition, and RE elements.

Our study, therefore, explored and compared the effect of Na, Fe, and Pr as representative alkali, transition, and RE metal dopants on the photocatalytic activity of g-C_3N_4 for the first time. The photocatalysts were prepared using the same synthetic method by only varying the dopant precursor selected. We adopted urea, as a suitable and economical precursor, for the synthesis of g-C_3N_4. The pre-formed g-C_3N_4 was then dispersed and mixed with the dopant precursor, and thermally exfoliated at 550 °C. This simple approach, via integration of ion intercalation and thermal treatment, was expected to produce dopant-modified g-C_3N_4 nanosheets. The performances of as-prepared g-C_3N_4 with modifiers were evaluated and compared through the photocatalytic degradation of MB under visible light. Their structural, chemical, optical, and photoelectrochemical properties were then investigated in detail to explore possible reasons contributing to their varying MB removal capacities. The Pr-doped g-C_3N_4 displayed the most promising photocatalytic activity as compared with the Na and Fe-doped g-C_3N_4. Its performance was investigated for different Pr loadings and different water environments, and was tested for reusability and stability. Lastly the related mechanism for photocatalytic reaction was proposed.

2 Experimental

2.1 Materials

Urea (99.7%), praseodymium(III) nitrate hexahydrate ($Pr(NO_3)_3{\cdot}6H_2O$, 99.9%), sodium hydroxide (97.0%), iron(III) chloride hexahydrate (> 99.5%), MB (dye content ⩾ 82%), RhB (dye content ⩾ 99.5%), methyl orange (MO, dye content ⩾ 85%), benzoquinone (BQ, > 98.0%), L-tryptophan (L-Trp. ⩾ 98.0%), sodium ethylenediaminetetraacetate (Na_2EDTA, > 99.0%), isopropyl alcohol (IPA, > 99.0%), 5,5-dimethyl-pyrroline N-oxide (DMPO, ⩾ 98.0%), 2,2,6,6-tetramethyl-piperidin-1-oxyle (TEMPO, ⩾ 98.0%), 2,2,6,6-tetramethyl-piperidine (TEMP, ⩾ 98.0%), and TritonX-100 (⩾ 70%) were purchased from Sigma-Aldrich. All chemicals, including HNO_3, Na_2SO_4, NaCl, $MgCl_2$, $AlCl_3$, and Na_2HPO_4, were used without further purification.

2.2 Preparation of bulk g-C_3N_4

Approximately 10 g of urea was thermally pyrolyzed in a ceramic crucible at a temperature of 550 °C for 2 h with a ramping of 10 °C·min^{-1}. After cooling down naturally, the material was crushed to obtain the bulk g-C_3N_4 powder.

2.3 Preparation of Pr(0.4)g-C_3N_4, Na(0.4)g-C_3N_4, and Fe(0.4)g-C_3N_4

To synthesize g-C_3N_4 samples doped with different elements, 0.2 g of bulk g-C_3N_4 was dispersed in 10 mL ultrapure water (Milli Q) containing 0.04 g of $Pr(NO_3)_3{\cdot}6H_2O$, sodium hydroxide, or iron chloride hexahydrate. The resulting suspension was sonicated for 0.5 h, magnetically stirred for 0.5 h, and then dried at 100 °C to yield a solid powder. Subsequently, the dried solid was treated at 550 °C for 1 h with a ramping of 10 °C·min^{-1} to obtain Pr(0.4)g-C_3N_4, Na(0.4)g-C_3N_4, or Fe(0.4)g-C_3N_4, respectively.

To optimize the performance of Pr-doped g-C_3N_4, the same procedures were utilized as above, except the addition of $Pr(NO_3)_3{\cdot}6H_2O$ was varied in the range of 0.01–0.12 g. Pr(x)g-C_3N_4 was synthesized, where x represents the mass (g) of the $Pr(NO_3)_3{\cdot}6H_2O$ added in the synthesis.

2.4 Characterization

The morphological characteristics of the pristine g-C_3N_4 and doped g-C_3N_4 samples were examined with a field emission scanning electron microscopy (FESEM, Tescan Clara). Transmission electron microscopy (TEM, FEI FS200X G2) in conjunction with energy dispersive X-ray spectroscopy was employed to study the microstructure and elemental compositions of the as-prepared samples. The chemical states of the elements were studied using X-ray photoelectron spectroscopy (XPS, Kratos AXIS Ultra DLD). The crystal structures of the samples were investigated with an X-ray diffraction diffractometer (XRD, Rigaku) in the 2θ range of 10°–80°. Fourier transform infrared spectroscopy (FTIR, PerkinElmer Frontier) was utilized to probe the sample chemical structures. The Brunauer-Emmett-Teller (BET) surface areas and porous structures of the samples were quantified using a SAPA 2010 micromeritics analyzer (Tristar II 3020). A UV-Vis diffuse reflectance spectrophotometer (UV-Vis DRS, PerkinElmer Lambda 650) with $BaSO_4$ reference attached to an integrating sphere accessor was employed to measure the optical

properties of the samples. The band gap was estimated from the Tauc plot of $(\alpha h\upsilon)^2$ *vs*. $h\upsilon$.

2.5 Photocatalytic activity measurement

The photocatalytic activity of the g-C_3N_4 and doped g-C_3N_4 was evaluated by photocatalytic degradation of MB. Typically, 20 mg of the photocatalyst was dispersed into 50 mL of 10 mg·L^{-1} MB aqueous solution in a cylindrical Pyrex glass container. The solution was first stirred for 30 min in the dark to establish an adsorption-desorption equilibrium. Subsequently, the photocatalytic degradation was initiated by exposing the suspension to the visible light, which was emitted by a xenon lamp (CEL-HX F300) with a cut-off filter (λ > 420 nm). The reaction was maintained for 40 min, while aliquots were taken at intervals of 10 min and centrifuged at 12000 r·min^{-1} for 5 min to separate the photocatalyst from the aqueous solution. The absorbance of the aqueous solution was determined at 664 nm on a Shimadzu UV/V is spectrophotometer. The organic removal rate of the photocatalyst was quantified using Eq. (1). The reaction kinetics were examined using Eq. (2) [20].

$$\text{Dye removal}\ (\%) = \left(1 - \frac{C}{C_0}\right) \times 100, \tag{1}$$

$$-\frac{\mathrm{d}C}{\mathrm{d}t} = kC, \tag{2}$$

where C_0, C, k, and t indicate the initial concentration (mg·L^{-1}), the concentration at a specific time (mg·L^{-1}), the rate constant of degradation (min^{-1}), and the time of reaction (min), respectively.

2.6 Photoelectrochemical measurements

Photocurrent density and electrochemical impedance spectroscopy (EIS) were examined using a Biologic SP-300 electrochemical workstation (Lambda System Biologic SP-300; applied potential: 0.5 V; time: 140 s; potential range: –2.5 to +2.5 V; bandwidth: 8) with a typical three-electrode setup. The fluorine-doped oxide (FTO)-coated catalyst, Ag/AgCl, and Pt were the working, reference, and counter electrodes. The working electrode was prepared as follows: 5 mg of catalyst was mixed with 10 μL of Trixton-100 and 20 μL of deionized water to form a slurry. Subsequently, the slurry was coated on a tape-masked FTO glass slide to achieve an uncovered active area of 1 cm^2 for the photocatalyst electrode. The coated FTO slides were dried at 350 °C for 45 min. Using a xenon lamp (CEL-HX F300) with a 420 nm cut-off filter, the photocurrent density in 0.1 mol·L^{-1} Na_2SO_4 electrolyte solution was determined with and without visible light illumination at intervals of 20 s. Also, the EIS analysis was performed under visible light illumination from 50 mHz to 100 kHz. Mott-Schottky tests were conducted at an alternating current voltage of 10 mV, a potential range of –1.0 to +1.0 V, and a frequency of 1000 Hz.

2.7 Reusability, stability, and identification of reactive species

To examine the reusability and stability of the photocatalyst, the repeated photocatalytic degradation (5) cycles of MB under similar reaction conditions were performed. After the 5th cycle, the crystal and chemical structures of the used photocatalyst were examined using XRD and FTIR analysis. To explore the key reactive species in the photocatalytic reaction, 5 mmol·L^{-1} of BQ, L-Trp., and Na_2EDTA were introduced into the reaction suspension as scavengers for superoxide ($\bullet O_2$), $^1O_2$, hydroxyl ($\bullet$OH), and holes (h^+), respectively. In addition, the reactive species were analytically studied by the electron spin resonance (ESR) spectroscopy using a Bruker ESR 300E with a microwave bridge.

3 Results and discussion

3.1 Performance and characteristics of Fe, Na, and Pr-doped g-C_3N_4

3.1.1 Performance of Pr(x)g-C_3N_4, Na(0.4)g-C_3N_4, and Fe(0.4)g-C_3N_4

To explore the impact of different dopants on the photocatalytic activity of g-C_3N_4, photocatalytic degradation tests for MB removal were conducted using g-C_3N_4, Na(0.4)g-C_3N_4, Fe(0.4)g-C_3N_4, and Pr(0.4)g-C_3N_4. Their MB removal rate after 30 min adsorption in the dark and 40 min photocatalytic reaction under visible light, and the corresponding first-order kinetic constants (k) are shown in Figs. 1(a) and 1(b). In general, the doping of g-C_3N_4 increased adsorptive ability for MB removal relative to g-C_3N_4; while it enhanced photocatalytic activity of g-C_3N_4 except for the introduction of Fe. Pr(0.4)g-C_3N_4 exhibited the most promising MB removal, with the highest adsorptive removal (~62%) in the dark and the greatest k value (0.108 min^{-1}). Despite an increase of MB adsorption before light irradiation, Fe(0.4)g-C_3N_4 exhibited no significant improvement in the total MB removal over g-C_3N_4 and had a k value of 0.021 min^{-1}, which was lower than that of g-C_3N_4 (0.033 min^{-1}).

3.1.2 Optimization of Pr(x)g-C_3N_4 by varying Pr doping

To optimize the MB removal performance as a function of Pr doping, the amount of $Pr(NO_3)_3 \cdot 6H_2O$ added during the synthesis of Pr(x)g-C_3N_4 was varied from 0.01 to 0.12 g (relative to 0.2 g of the pre-formed g-C_3N_4). The

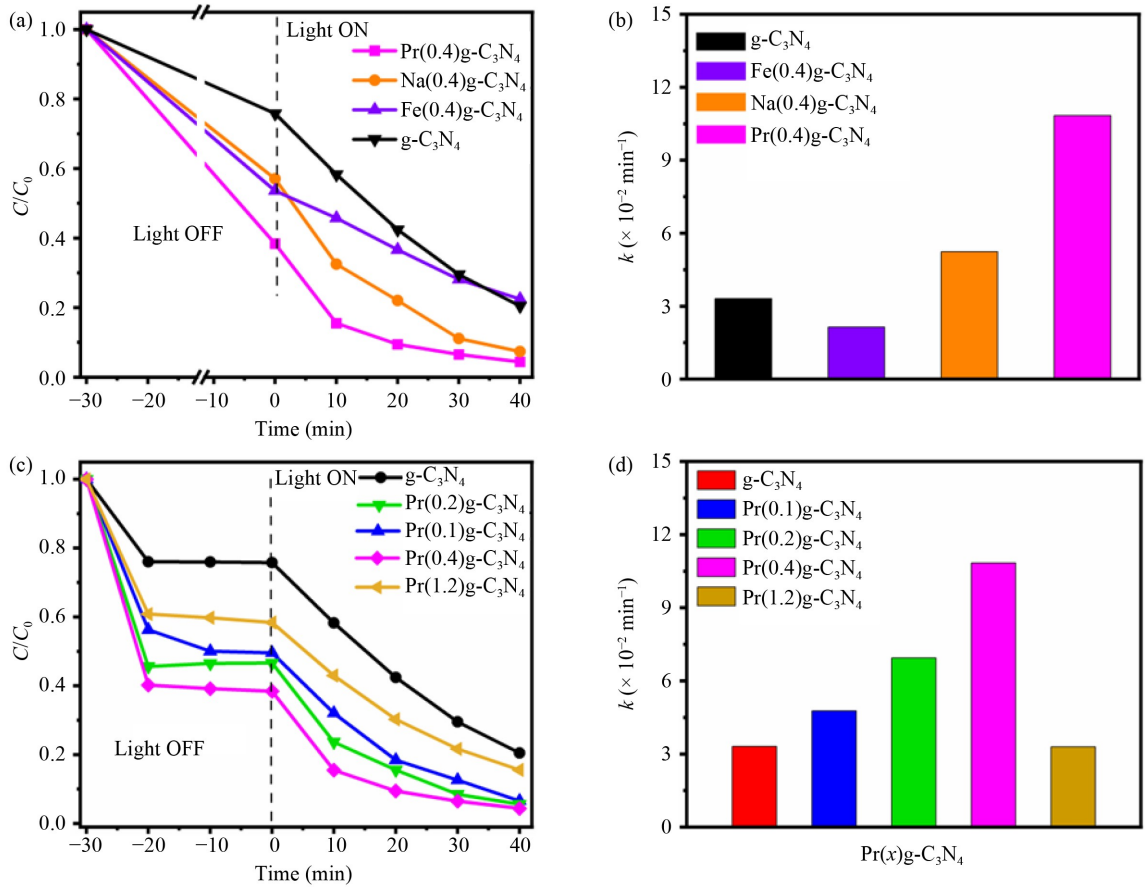

Fig. 1 (a) Photocatalytic degradation performance and (b) corresponding pseudo-first-order rate constants (k) of g-C_3N_4, Na(0.4)g-C_3N_4, Fe(0.4)g-C_3N_4, and Pr(0.4)g-C_3N_4, as compared to g-C_3N_4 (temperature = 25 °C; initial MB concentration = 10 mg·L^{-1}; catalyst dosage = 0.4 g·L^{-1}; initial pH = 5.37). (c) Photocatalytic degradation performance and (d) corresponding pseudo-first-order rate constants (k) of g-C_3N_4, Pr(0.1)g-C_3N_4, Pr(0.2)g-C_3N_4, Pr(0.4)g-C_3N_4, and Pr(1.2)g-C_3N_4 (temperature = 25 °C; initial MB concentration = 10 mg·L^{-1}; catalyst dosage = 0.4 g·L^{-1}; initial pH = 5.37).

resulting samples of Pr(x)g-C_3N_4 were designated as Pr(0.1)g-C_3N_4, Pr(0.2)g-C_3N_4, Pr(0.4)g-C_3N_4, and Pr(1.2)g-C_3N_4, respectively. Figures 1(c) and 1(d) compare the photocatalytic performance and the pseudo-first-order kinetic rates (k) of Pr(x)g-C_3N_4 and the pristine g-C_3N_4 for the removal of MB. It should be noted that the fast adsorption of MB onto the pristine and modified g-C_3N_4 reached equilibrium within 10 min in the dark. Overall, the Pr doping of g-C_3N_4 led to a better MB removal rate than that for g-C_3N_4 (79.6%) (Fig. 1(c)). The kinetic rate constant (k), representing the rate of the reaction catalyzed by the photocatalyst, is often used as an indicator to evaluate the catalyst activity. Specifically, the greater kinetic rate constant (k), the greater photocatalytic activity. The k was also seen to be greater when using Pr(x)g-C_3N_4 in the photocatalytic reaction, with the order of Pr(0.4)g-C_3N_4 (0.108 min^{-1}) > Pr(0.2)g-C_3N_4 (0.069 min^{-1}) > Pr(0.1)g-C_3N_4 (0.048 min^{-1}) > Pr(1.2)g-C_3N_4 (0.033 min^{-1}) ~g-C_3N_4 (0.033 min^{-1}). Therefore, Pr(0.4)g-C_3N_4, which was synthesized by mixing 0.04 g $Pr(NO_3)_3{\cdot}6H_2O$ and 0.2 g bulk g-C_3N_4 ($Pr(NO_3)_3{\cdot}6H_2O$/bulk g-C_3N_4 mass ratio of 1/5) was adopted as the optimum photocatalyst. The observed improved MB removal rate for Pr(x)g-C_3N_4 could be attributed to both the improved adsorption in the dark and enhanced photocatalytic reaction under visible light. In particular, the MB total removal of Pr(x)g-C_3N_4 was enhanced by increasing the amount of Pr dopant (e.g., 93.4% for Pr(0.1)g-C_3N_4, 94.4% for Pr(0.2)g-C_3N_4, and 95.6% for Pr(0.4)g-C_3N_4). However, a high loading of Pr dopant (i.e., Pr(1.2)g-C_3N_4) resulted in a decline in the total MB removal (84.4%). This may be due to the recombination of photogenerated holes and electrons over the excess Pr dopant [21,22]. Meanwhile, we speculated that the excessive Pr loading might lead to the agglomeration of dopants and/or covering of the active sites on the g-C_3N_4 surface, thereby reducing the amount of available active sites and efficiency of charge separation [21,22]. The following characterizations support this hypothesis.

3.1.3 Characterization of Pr(x)g-C_3N_4, Na(0.4)g-C_3N_4, and Fe(0.4)g-C_3N_4

Various doped g-C_3N_4 catalysts were examined in detail to explore the correlation between their performances and

characteristics, including crystal, chemical, textural, optical, and photoelectrochemical characteristics. The FTIR spectra (Figs. 2(a) and 2(b)) of the g-C_3N_4 and doped g-C_3N_4 revealed a band at 810 cm^{-1}, which is attributable to the bending vibration of the *s*-triazine ring of g-C_3N_4. The prominent bands at 1200–1640 cm^{-1} are associated with the stretching vibration modes of C=N and C–N; while those at 2971–3390 cm^{-1} are related to –NH–, $–NH_2$, and –OH (from adsorbed water) [9]. All these bands were observed in the FTIR spectra of g-C_3N_4 and doped g-C_3N_4, indicating that the chemical structure of g-C_3N_4 was largely preserved after various metal doping or varying Pr doping. As for Fe(0.4)g-C_3N_4, the characteristic bands at 476 and 557 cm^{-1}, corresponding to the stretching vibration of the Fe–O bond, were observed. This revealed the presence of Fe dopants (i.e., Fe_2O_3) in the Fe(0.4)g-C_3N_4 [23].

Figure 2(c) shows the XRD patterns of g-C_3N_4 and doped g-C_3N_4. Two main peaks at 13.1° and 27.3° are ascribed to the (100) and (002) diffraction planes, representing the in-plane periodic stacking of tri-*s*-triazine and the interlayer stacking of conjugate aromatic rings in g-C_3N_4. A reduced intensity of the peaks at 13.1° and 27.3° was seen for the doped g-C_3N_4 relative to the pristine g-C_3N_4, which may be due to the host-guest interaction, which distorts the crystallinity and order of parent g-C_3N_4 structure [24]. This was also observed when increasing the Pr loading in the g-C_3N_4 (Fig. 2(d)). Figure S1 (cf. Electronic Supplementary Material, ESM) shows a slight increase in the diffraction angle of the (002) peak in the modified g-C_3N_4 relative to the bulk g-C_3N_4, implying the formation of a compact structure with reinforced intermolecular forces between the metal dopants and the host material, which is similar to the results in literature [25]. The decrease in the peak intensity and slightly positive shift of the (002) diffraction peak in the metal-doped g-C_3N_4 reveal the formation of more compact atomic layers and a lower number of nanosheets relative to the bulk g-C_3N_4, attributable to the synergy between thermal treatment and metal doping. The reduced interlayer stacking distance in the metal-doped g-C_3N_4 would be beneficial for the migration of photogenerated charge carriers [26]. The plane (100) can be seen to persist in the samples of Pr(0.4)g-C_3N_4 and Na(0.4)g-C_3N_4 in Fig. 2(c). Figure S2 (cf. ESM) shows the existence of the (100) plane even at a higher Pr doping level, as observed in the XRD pattern of Pr(1.2)g-C_3N_4. It should be noted that no apparent new peaks were observed in the XRD patterns of Pr(*x*)g-C_3N_4 and Na(0.4)g-C_3N_4, suggesting high dispersity of dopants on g-C_3N_4. However, the (100) diffraction peak was not apparent in the XRD pattern of Fe(0.4)g-C_3N_4, which may suggest the doping of the Fe species into the in-planes of g-C_3N_4 or restacking along the (100) direction of g-C_3N_4 nanosheets [8]. Moreover, the peaks with high intensity occurring at 33.0° and 35.5° are attributable to highly crystalline Fe_2O_3, implying crystallization of Fe ion dopant into oxide [27], possible agglomeration, and uneven doping.

The micro-textures of the pristine g-C_3N_4 and doped g-C_3N_4 samples were examined by nitrogen adsorption-desorption analysis (Figs. 2(e) and 2(f), and Table 1). All

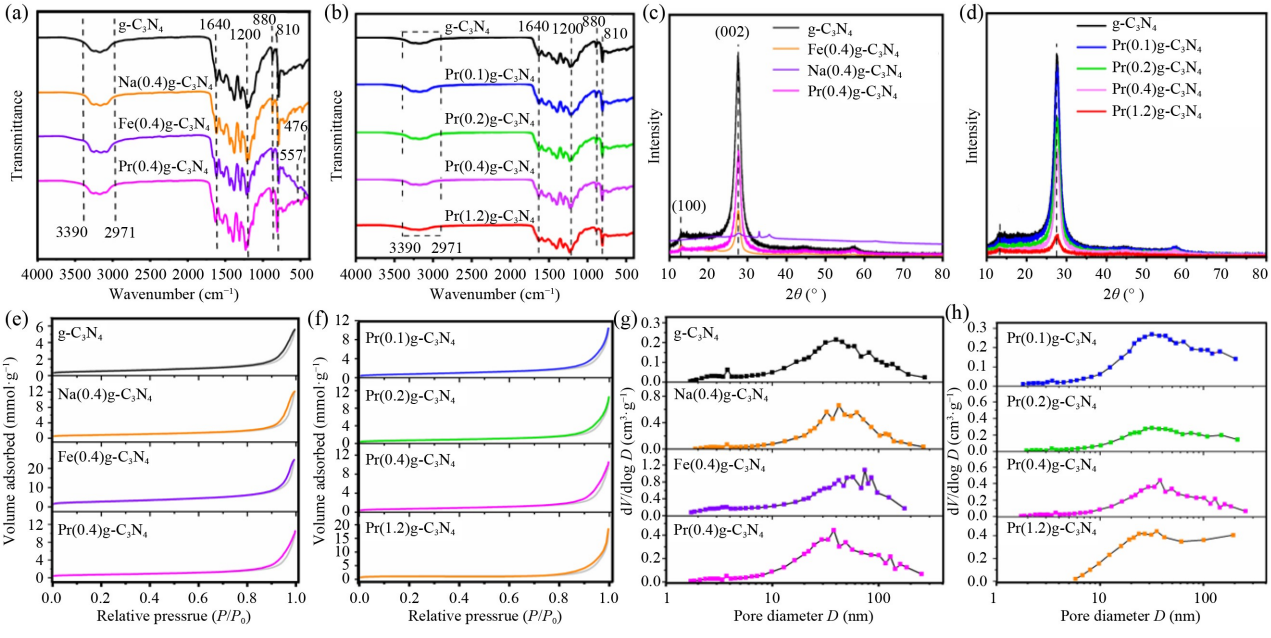

Fig. 2 (a) FTIR spectra, (c) XRD patterns, (e) nitrogen adsorption-desorption isotherm curves, and (g) Barret-Joyner-Halenda (BJH) pore size distribution curves of g-C_3N_4, Na(0.4)g-C_3N_4, Fe(0.4)g-C_3N_4, and Pr(0.4)g-C_3N_4; (b) FTIR spectra, (d) XRD patterns, (f) nitrogen adsorption-desorption isotherm curves, and (h) BJH pore size distribution curves of Pr(0.1)g-C_3N_4, Pr(0.2)g-C_3N_4, Pr(0.4)g-C_3N_4, and Pr(1.2)g-C_3N_4.

Table 1 Micro-textural properties of g-C_3N_4, Na(0.4)g-C_3N_4, Fe(0.4)g-C_3N_4, and Pr(x)g-C_3N_4 (x = 0.1, 0.2, 0.4, and 1.2)

Photocatalyst	BET surface area ($m^2 \cdot g^{-1}$)	Pore volume ($cm^3 \cdot g^{-1}$)	Pore diameter (nm)
g-C_3N_4	41.7	0.192	18.6
Na(0.4)g-C_3N_4	66.2	0.417	27.2
Fe(0.4)g-C_3N_4	221.1	0.829	16.3
Pr(0.4)g-C_3N_4	56.8	0.344	23.6
Pr(0.1)g-C_3N_4	43.9	0.291	24.5
Pr(0.2)g-C_3N_4	49.4	0.312	24.8
Pr(0.4)g-C_3N_4	56.8	0.344	23.6
Pr(1.2)g-C_3N_4	78.5	0.628	37.1

the samples revealed a typical IV adsorption isotherm curve with an H3 hysteresis loop (Figs. 2(e) and 2(f)). This confirmed the presence of mesoporous structures, which was further validated by the pore size distribution in Figs. 2(g) and 2(h). Figures 2(g) and 2(h) also demonstrate an increase in the porosity of g-C_3N_4 upon doping with Na, Fe, or Pr. In Table 1, Fe(0.4)g-C_3N_4 exhibited the highest BET surface area (221.1 $m^2 \cdot g^{-1}$) and pore volume (0.829 $cm^3 \cdot g^{-1}$), possibly due to the Fe doping into the in-planes of g-C_3N_4 and restacking along the (100) direction (as suggested by the XRD results), and the formation of Fe_2O_3 nanoparticles on the surfaces of g-C_3N_4 (as evidenced by the later SEM observation). However, we noted that the pore size of the Fe-doped sample (16.3 nm) was smaller than that of the Na or Pr-doped and pristine g-C_3N_4. This might be due to excessive Fe dopants forming particles (aggregates) on the surfaces or/and partially covering the gaps or pores of g-C_3N_4 stacks.

The sample of g-C_3N_4 was observed to have irregular thickness with agglomeration of spongy-like sheets in the SEM image (Fig. 3(a)). The metal dopants impacted the graphitic morphology differently, as shown in Figs. 3(b)–3(d). The as-prepared Na(0.4)g-C_3N_4 displayed nanosheets with thin layers comparable to the g-C_3N_4 (Fig. 3(b)), suggesting that the dopants did not significantly affect the morphology. Conversely, an apparent loss of the graphitic nanosheet morphology was seen in Fig. 3(c) for Fe(0.4)g-C_3N_4; aggregates were formed, which might be due to the formation of Fe_2O_3. This was further supported by the XRD results, which revealed a loss of the g-C_3N_4 facets (100) and (002) with the formation of peaks attributable to Fe_2O_3 particles (Fig. 2(c)). Interestingly, the Pr(0.4)g-C_3N_4 was characterized by porous flattened nanosheets with thin irregular curved edges (Fig. 3(d)), which were later identified with the facets corresponding to Pr_6O_{11} (Fig. 4(b)). By increasing the loading of Pr into Pr(x)g-C_3N_4, a transformation of the morphology of typical carbon nitride spongy-like sheets into that of more flattened nanosheets was observed. The tapering of the nanosheets was observed to be more prominent with an increase in Pr dopants; from Pr(0.1)g-C_3N_4 (Fig. 3(e)), Pr(0.2)g-C_3N_4 (Fig. 3(f)) to Pr(0.4)g-C_3N_4 (Fig. 3(d)). A gradual increase of pore formation was also surprisingly seen from g-C_3N_4 (Fig. S3(a), cf. ESM), Pr(0.1)g-C_3N_4 (Fig. S3(b), cf. ESM), Pr(0.2)g-C_3N_4 (Fig. S3(c), cf. ESM) to Pr(0.4)g-C_3N_4 (Fig. S3(d), cf. ESM). The observed transformation of the morphology may be associated with the synergistic effect of high-temperature treatment and the Pr doping, which caused the exfoliation and peeling of the bulk g-C_3N_4 nanosheets. However, the further increase of dopant amount (e.g., in Pr(1.2)g-C_3N_4) did not appear to cause additional peeling of nanosheets and even led to some aggregate formation (Fig. 3(g)). It should be

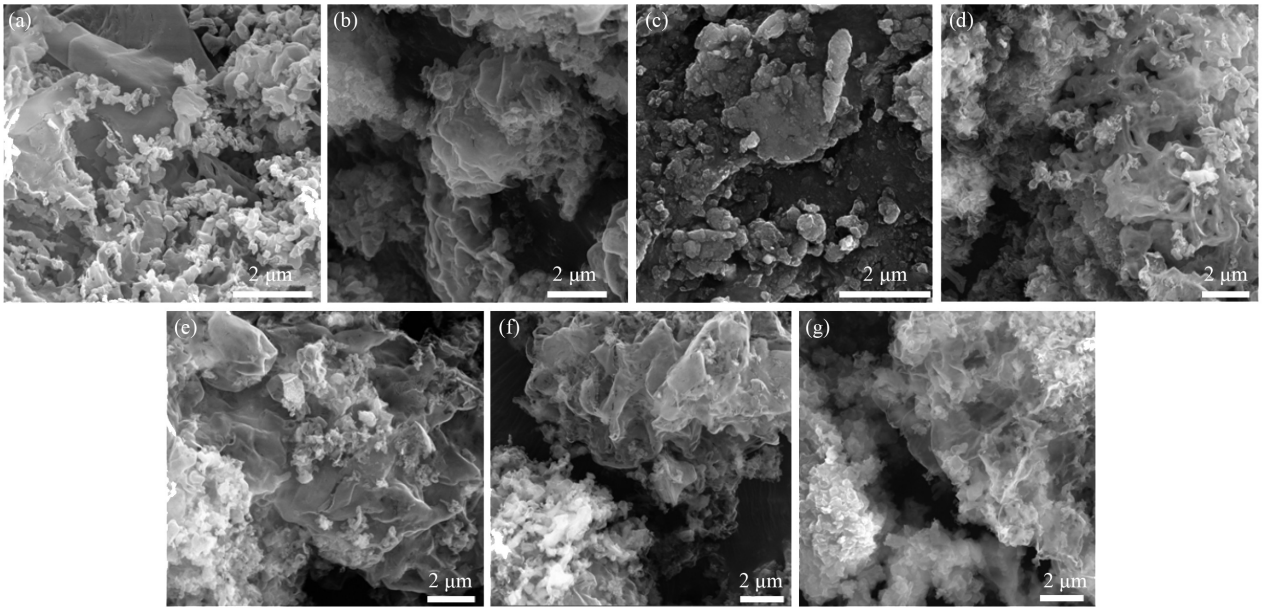

Fig. 3 SEM images of (a) g-C_3N, (b) Na(0.4)g-C_3N_4, (c) Fe(0.4)g-C_3N_4, (d) Pr(0.4)g-C_3N_4, (e) Pr(0.1)g-C_3N_4, (f) Pr(0.2)g-C_3N_4, and (g) Pr(1.2)g-C_3N_4.

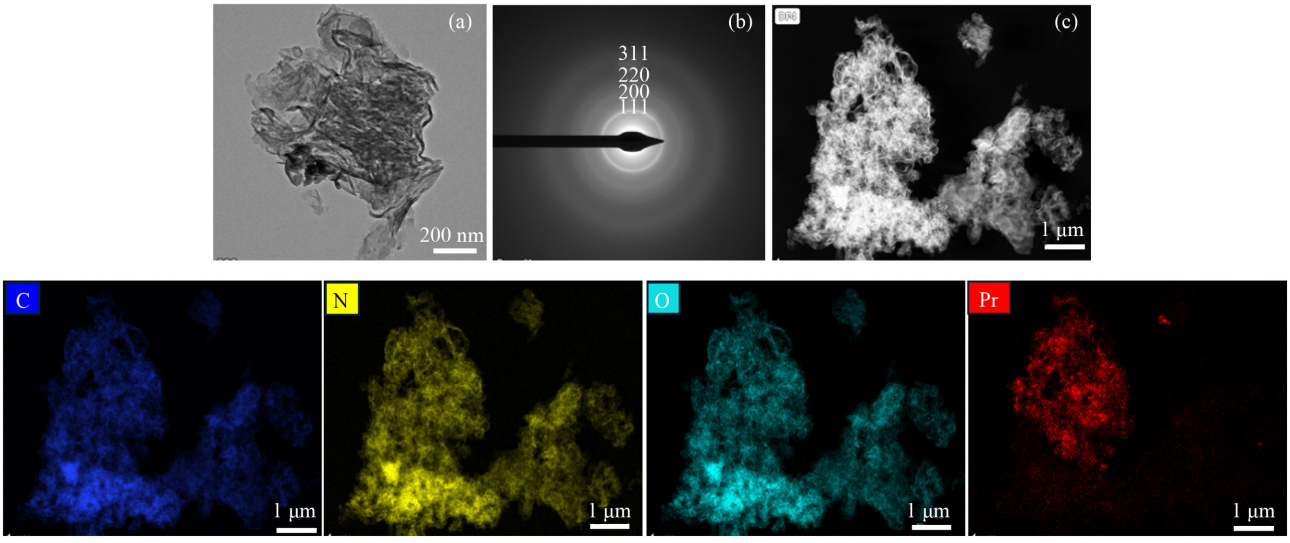

Fig. 4 (a) TEM image, (b) SAED, and (c) HAADF and EDS mapping of C, N, O, and Pr of Pr(0.4)g-C_3N_4.

noted that an apparent porous structure was formed in Pr(0.4)g-C_3N_4. Such a unique morphology of porous nanosheets in Pr(0.4)g-C_3N_4 would potentially improve its photocatalytic activity to remove organics from water.

Figure 4 details the microstructure of Pr(0.4)g-C_3N_4, which showed the best photocatalytic performance (Figs. 1(a) and 1(c)), using TEM. Figure 4(a) shows the nanosheet structure (g-C_3N_4) with some dark spots, which are believed to be the clusters of Pr dopants [17]. The selective area electron diffraction (SAED) analysis in Fig. 4(b) reveals the co-existence of Pr dopants, that the (111), (200), (220), and (311) planes of Pr_6O_{11}, as the most stable oxide form of Pr, were seen [17,28]. A uniform distribution of the Pr dopants was confirmed by the high-angle annular dark-field (HAADF) and energy dispersive spectroscopy (EDS) mapping analysis (Fig. 4(c)).

Figure S4 (cf. ESM) provides an XPS survey spectrum showing the elements present in Pr(0.4)g-C_3N_4. The peaks were unique to C, O, N, and Pr, aligning with the EDS elemental mapping analysis result (Fig. 4(c)). In Fig. 5(a), the deconvoluted high-resolution C 1s spectrum displays three peaks with the binding energies of 284.7, 289.1, and 291.6 eV. The peak at 284.7 eV is ascribed to the adventitious carbon (–C–C–/–C=C–) of graphitic carbon nitride from incomplete polymerisation, while the 289.1 eV is due to the aromatic carbon atoms (N–C=N) [29]. The peak with the binding energy of 291.6 eV is associated with the (–C=O) [29]. The deconvolution of N 1s spectrum reveals three peaks with binding energy of 399.6, 402.0, and 403.7 eV, which correspond to –C=N–C, N–$(C)_3$, and C–N–H, respectively (Fig. 5(b)). Figure 5(c) shows the O 1s spectrum with three peaks at 528.0, 533.1, and 536.1 eV, indicating the presence of lattice oxygen atoms on the Pr dopants, C–O and oxygen from surface-adsorbed water [17,30]. The Pr 3d spectrum in Fig. 5(d) displays Pr $3d_{5/2}$ and Pr $3d_{3/2}$ peaks due to the presence of Pr^{3+} in Pr_6O_{11} [30]. The deconvoluted Pr $3d_{3/2}$ and $3d_{5/2}$ peaks show the main/satellite peaks at binding energies of 957.7/960.6 and 937.3/941.4 eV, respectively.

Fe(0.4)g-C_3N_4, Na(0.4)g-C_3N_4, and Pr(0.4)g-C_3N_4 displayed improved visible light absorption relative to the pristine g-C_3N_4 (464 nm), as shown in Fig. 6(a). In particular, Fe(0.4)g-C_3N_4 showed the most extensive redshift toward the visible light region of the electromagnetic spectrum. The order of increasing visible light absorption edge was Fe(0.4)g-C_3N_4 > Na(0.4)g-C_3N_4 > Pr(0.4)g-C_3N_4 > g-C_3N_4. The corresponding band gap energy of the samples was calculated from the Tauc plot of $(\alpha h\nu)^2$ *vs.* energy ($h\nu$) (Fig. 6(b)). The band gap energy of g-C_3N_4 was narrowed upon metal doping, especially with Fe dopants. We also explored an improved visible light absorption response and a corresponding narrowing of E_g for Pr(x)g-C_3N_4 by increasing Pr loading (e.g., from Pr(0.1)g-C_3N_4 to Pr(0.4)g-C_3N_4) in Figs. 6(c) and 6(d). Excessive Pr doping, such as in Pr(1.2)g-C_3N_4, decreased the visible absorption to ca. 477 nm and light absorption intensity, which could be due to inhibition of the visible light penetration. Figure 6(e) estimates the flat-band potential (E_{FB}) for the g-C_3N_4, Fe(0.4)g-C_3N_4, Na(0.4)g-C_3N_4, and Pr(0.4)g-C_3N_4 using the Mott-Schottky analysis. The positive slopes of the Mott-Schottky plots imply that all the as-prepared samples are *n*-type semiconductors. Except for Pr(0.4)g-C_3N_4, a positive shift in E_{FB} relative to that of g-C_3N_4 was noticed in those metal-doped samples. For an n-type semiconductor, the conduction band (CB) is 0.1 V more negative than the E_{FB}. Therefore, the E_{FB} (the corresponding E_{CB}; E_{NHE} = Ag/AgCl + 0.197, NHE: normal hydrogen electrode) of g-C_3N_4, Na(0.4)g-C_3N_4, Fe(0.4)g-C_3N_4, and Pr(0.4)g-C_3N_4, was computed to be –0.64 V (–0.54 eV), –0.53 V (–0.43 eV), –0.55 V (–0.45 eV), and –0.69 V (–0.59 eV),

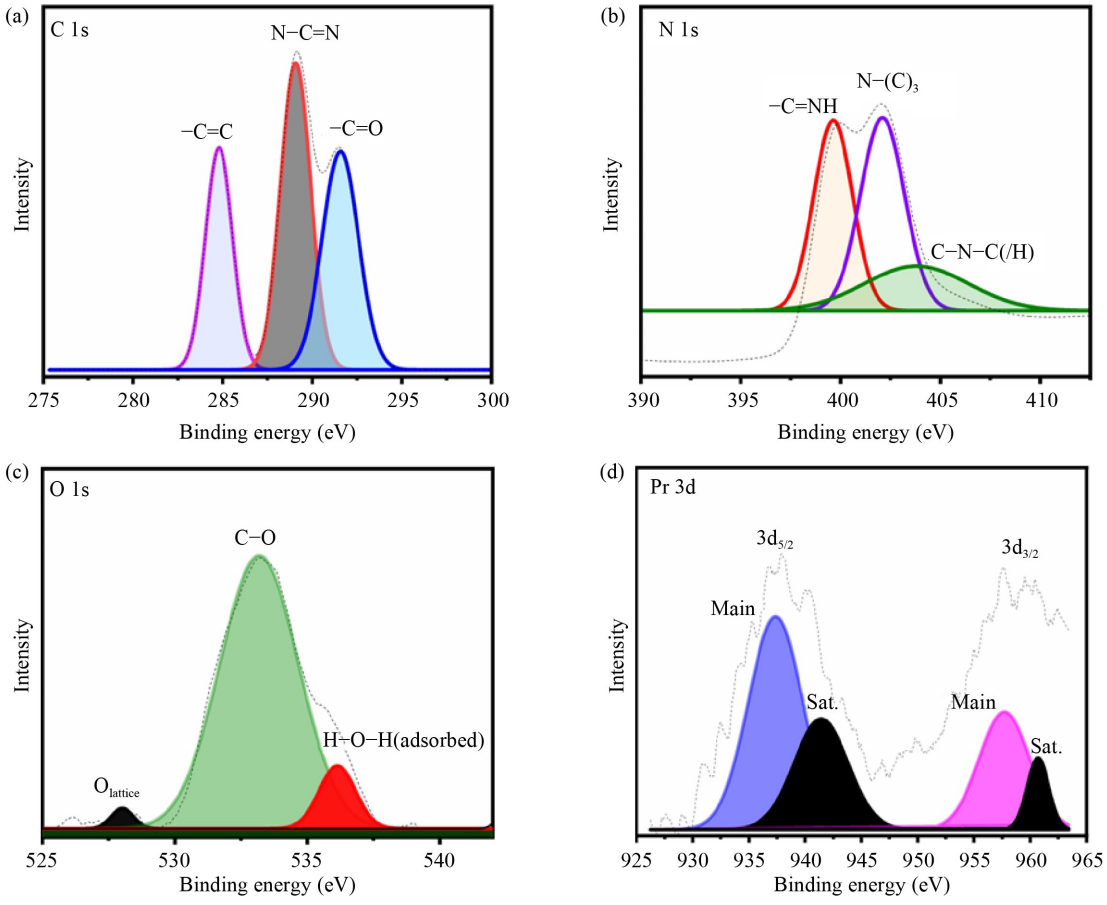

Fig. 5 XPS analysis of Pr(0.4)g-C_3N_4: (a) C 1s, (b) N 1s, (c) O 1s, and (d) Pr 3d.

respectively. The associated valence potential (E_{VB}) was calculated using the equation $E_{VB} = E_{CB} + E_g$. The E_{VB} of g-C_3N_4, Na(0.4)g-C_3N_4, Fe(0.4)g-C_3N_4, and Pr(0.4)g-C_3N_4 was separately estimated to be +2.20, +2.21, +1.33, and +2.04 eV, respectively. Figure 6(f) summarizes the electronic structures of g-C_3N_4, Na(0.4)g-C_3N_4, Fe(0.4)g-C_3N_4, and Pr(0.4)g-C_3N_4. It should be noted that Pr(x)g-C_3N_4, especially with low Pr doping, demonstrated greater visible light absorption activity and narrower band gaps than g-C_3N_4, thereby potentially would have improved effectiveness for the photocatalytic remediation of organics.

Figure S5 (cf. ESM) shows the charge carrier density (N_D) of g-C_3N_4, Na(0.4)g-C_3N_4, Fe(0.4)g-C_3N_4, and Pr(0.4)g-C_3N_4; that all the doped samples showed higher N_D, suggesting that metal doping can increase the number of charge carriers and boost the photoactivity of the material. The relatively large N_D of Na(0.4)g-C_3N_4 may be associated with its higher chemical activity than other metal dopants. Meanwhile, the lower N_D of Fe(0.4)g-C_3N_4 than that of Pr(0.4)g-C_3N_4 may be due to the weakened g-C_3N_4 structure. It might also be largely attributed to the excessive loading of Fe dopants, which caused uneven distribution and aggregation of Fe_2O_3, interfering with charge migration [31]. In Fig. 7(a), higher photocurrent density was observed in the metal-doped samples over g-C_3N_4, implying better separation and transfer of photogenerated charge carriers. Figure 7(b) shows the Nyquist plots for the charge transfer resistance of the photocatalysts. The photocatalyst electrolyte interface behavior was explored by fitting the Nyquist plots to the equivalent circuit (Fig. S6, cf. ESM), where R_s, R_p, R_{ct}, W, and Q denote the electrolyte resistance, pore resistance, charge transfer resistance, Warburg impedance, and constant phase element, respectively. The R_{ct} value of Fe(0.4)g-C_3N_4 (633.2 Ω), Na(0.4)g-C_3N_4 (45.3 Ω), and Pr(0.4)g-C_3N_4 (5.3 Ω) was lower than of the g-C_3N_4 (1250 Ω), which corroborates the better charge transfer and higher photocurrent density observed in the metal-doped samples. The observed electrochemical properties of the metal-doped samples revealed improvements over g-C_3N_4 in terms of charge carrier density, charge separation, and transfer. In particular, Pr(0.4)g-C_3N_4 exhibited the best improvement in charge carrier density and photocurrent density, with the most significantly reduced charge transfer resistance.

3.1.4 Proposed structure and performance of Pr(0.4)g-C_3N_4, Na(0.4)g-C_3N_4, and Fe(0.4)g-C_3N_4

Based on the literature, there are two possible interactions between metal dopants and crystal structure of g-C_3N_4,

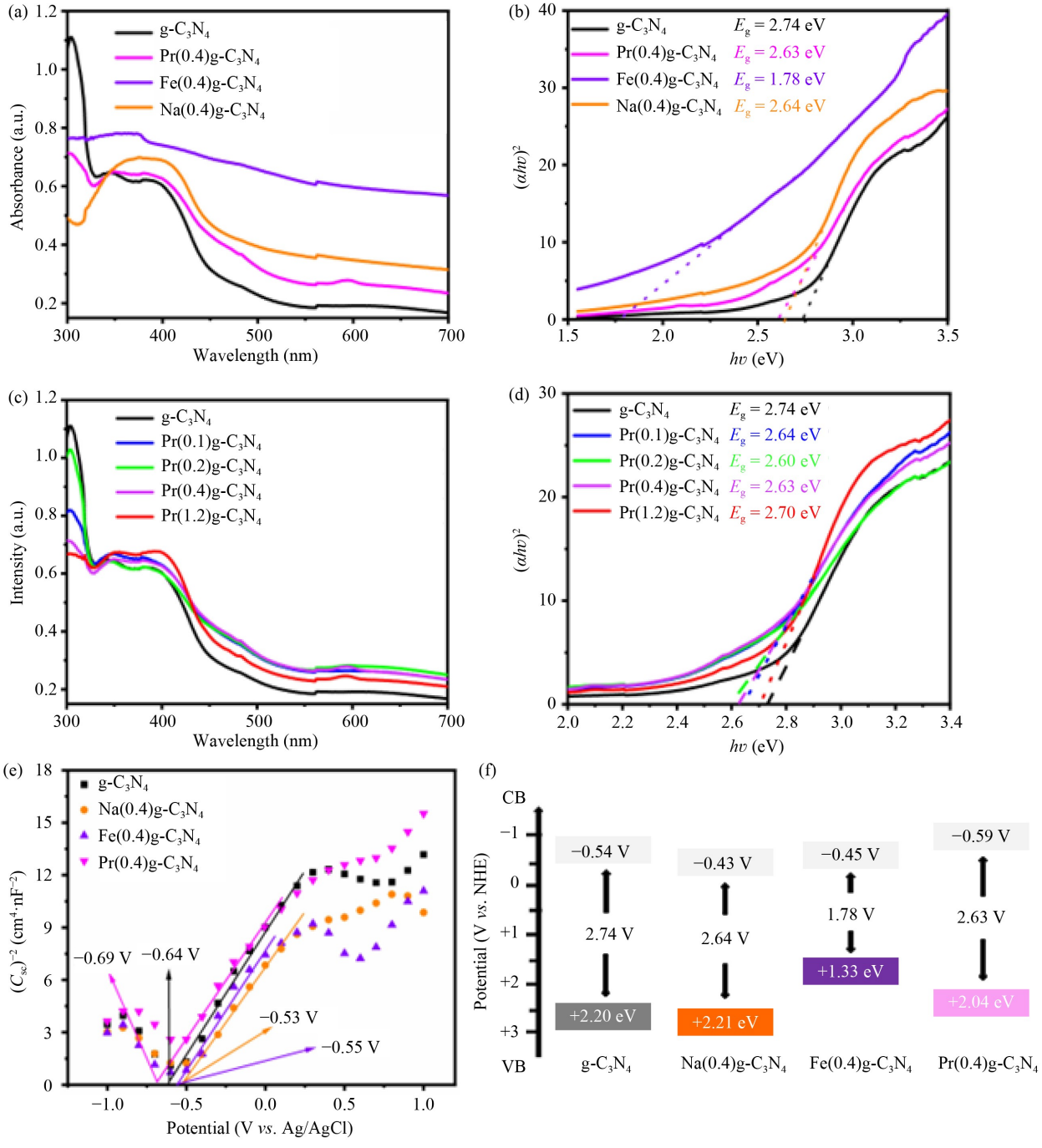

Fig. 6 (a) UV-Vis DRS spectra, (b) corresponding Tauc plots, (e) Mott-Schottky plots, and (f) electronic structures of g-C_3N_4, Na(0.4)g-C_3N_4, Fe(0.4)g-C_3N_4, and Pr(0.4)g-C_3N_4; (c) UV-Vis DRS spectra and (d) corresponding Tauc plots of g-C_3N_4, Pr(0.1)g-C_3N_4, Pr(0.2)g-C_3N_4, Pr(0.4)g-C_3N_4, and Pr(1.2)g-C_3N_4.

which depend on the atomic radius of dopant relative to C and/or N of the g-C_3N_4. The replacement of C or N with a dopant can occur in g-C_3N_4 when the dopant size is similar to the atomic radius of C (0.77 Å) or N (0.70 Å); while intercalation may occur when the dopant atomic radius is greater than that of C or N. Based on the above characterization, the three metal dopants in this study were proposed to coordinate with atoms of g-C_3N_4 via the interplanar and interlayer nanosheets (Figs. S7(b) and S7(c), cf. ESM), since the atomic radii of Na (1.02 Å), Fe (1.24 Å), and Pr (2.47 Å) are larger than that of C or N [32−34]. The interlayer spacing of g-C_3N_4 and the metal-doped g-C_3N_4 samples were estimated using Bragg's equation: $2d\sin\theta = n\lambda$ (d = crystal plane spacing, n = order of diffraction, λ = wavelength of incident X-rays, and θ = Bragg's angle). The decrease in the interlayer spacing due to metal intercalation with planar nanosheets of g-C_3N_4 was deduced to be in the order g-C_3N_4 >

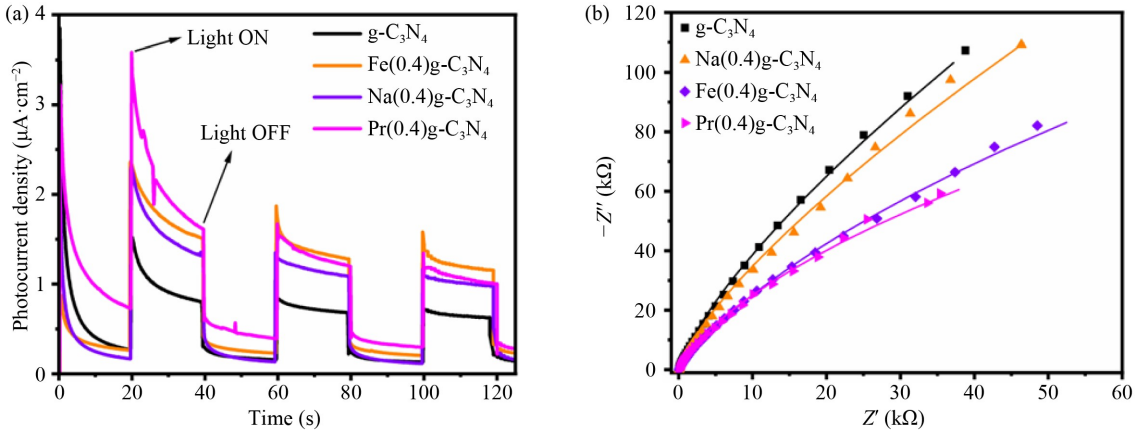

Fig. 7 (a) Transient photocurrent density and (b) Nyquist plots of g-C_3N_4, Na(0.4)g-C_3N_4, Fe(0.4)g-C_3N_4, and Pr(0.4)g-C_3N_4.

Na(0.4)g-C_3N_4 > Pr(0.4)g-C_3N_4 > Fe(0.4)g-C_3N_4, as depicted in Fig. S7 (cf. ESM). The Na ion was suggested to coordinate with the N atoms of the host g-C_3N_4 structure [24,35]. The Na ions in g-C_3N_4 could be used as channels for electron migration, enhancing the charge separation and thereby improving the photocatalytic performance of g-C_3N_4 [6,24]. Furthermore, the reduced peak intensity of (100) plane in Na(0.4)g-C_3N_4 (Fig. 2(c)) suggests partial coordination of Na with g-C_3N_4 via the interplanar atoms (Fig. S7(b), cf. ESM). On the other hand, the Fe and Pr dopants formed the heterostructure of Fe_2O_3 [36,37] or Pr_6O_{11} [17] and g-C_3N_4, respectively, as shown in Figs. S7(c) and S7(d) (cf. ESM). From the XRD pattern (Fig. 2(c)), the (100) plane of Fe-(0.4)g-C_3N_4 significantly diminished, implying less predominant interplanar coordination between g-C_3N_4 nanosheets but rather obvious coordination with the Fe_2O_3 dopants (Fig. S7(c), cf. ESM). Moreover, the SEM image of Fe(0.4)g-C_3N_4 (Fig. 3(c)) revealed a non-uniform distribution of irregularly shaped Fe_2O_3 aggregates on the g-C_3N_4. As for Pr(0.4)g-C_3N_4, the decrease in the peak intensity of (100) plane hints at a partial coordination of Pr_6O_{11} with g-C_3N_4 via the interplanar atoms (Fig. S7(d), cf. ESM)). The TEM image suggests a uniform distribution of Pr_6O_{11} on the g-C_3N_4 without aggregate formation, as evidenced by the SEM image (Fig. 3(d)).

As shown in Fig. 1, the metal-doped samples exhibited better adsorptive and photocatalytic performances than g-C_3N_4, in which Pr(0.4)g-C_3N_4 was the most promising. Despite the moderate improvement in terms of BET surface area, Pr(0.4)g-C_3N_4 exhibited the best photoelectrochemical properties with superior photocurrent response and charge carrier density, and reduced charge transfer resistance, along with the unique structure of porous nanosheet. We also noted the least improved total removal rate when using Fe(0.4)g-C_3N_4, especially the lowest k among different doped and pristine g-C_3N_4. Although its adsorptive capacity of MB, photocurrent response, and charge carrier density showed some improvement with lower resistance, the recombination of charge carriers might not be efficiently reduced, due to the significant loss of the crystal structure of g-C_3N_4 and apparent agglomeration of dopants, which could act as recombination sites or cover active sites.

The structures and photocatalytic reaction mechanisms for g-C_3N_4 with different dopants were proposed. In Na(0.4)g-C_3N_4, the Na species introduced impurities into g-C_3N_4 [6]; while the hybridization g-C_3N_4 with Na dopant could tune the electronic structure, VB, and CB. Upon visible light illumination, the Na dopants aid the separation and transfer of charge carriers to produce reactive oxygen species for degradation, as depicted in Fig. S8(a) (cf. ESM). On the other side, based on the Figs. 2 and 3, Fe and Pr dopants were proposed to form metal oxides, resulting in heterostructures with g-C_3N_4. The sample of Fe(0.4)g-C_3N_4 demonstrated a S-scheme heterostructure of g-C_3N_4/Fe_2O_3 (Fig. S8(b), cf. ESM)). The charge separation was facilitated by the interaction of the CB electrons of Fe_2O_3 and the VB holes of g-C_3N_4, which free up the CB electrons of g-C_3N_4 and the VB holes of Fe_2O_3 for reaction [37]. For Pr(0.4)g-C_3N_4, the Pr_6O_{11} was inactive to visible light due to its large band gap (> 3.15 eV); however, it could attract electrons from the CB of Pr(0.4)g-C_3N_4 [17]. The most plausible structure is shown in Fig. S8(c) (cf. ESM), in which Pr_6O_{11} accepts the photogenerated CB electrons from g-C_3N_4 [17]. The accumulated electrons on the surface of Pr_6O_{11} and the VB holes of g-C_3N_4 were utilized to degrade pollutants.

3.1.5 Comparison on the performance among Pr(0.4)g-C_3N_4, Na(0.4)g-C_3N_4, and Fe(0.4)g-C_3N_4 with the literature

Table S1 (cf. ESM) compares the photocatalytic performance of our Pr(0.4)g-C_3N_4, Na(0.4)g-C_3N_4, and Fe(0.4)g-C_3N_4 to other photocatalysts which have been reported in the literature. As discussed in Section 3.1.1, Pr(0.4)g-C_3N_4 exhibited the best MB removal rate with the highest adsorption (~62%) in the dark and the greatest k value (0.108 min^{-1}) among Pr(0.4)g-C_3N_4, Na(0.4)g-

C_3N_4, and Fe(0.4)g-C_3N_4. On the other side, the use of Pr(0.4)g-C_3N_4 could achieve a high and fast degradation > 95% MB removal within 40 min, when compared with other photocatalysts in the literature (listed in Table S1, cf. ESM) which showed reduced removal efficiency and prolonged reaction time. This promising performance of Pr(0.4)g-C_3N_4 would potentially reduce the treatment time and reactor size, thereby decreasing cost of operation when being scaled up to industrial application. It should also be noted that the synthetic route which was utilized to prepare Pr(0.4)g-C_3N_4 was simple, which can enable the possibility of large-scale synthesis, in contrast to the relatively complicated methods for preparing some of the photocatalysts, such as MnO_2/g-C_3N_4/ZnO [38], Ce-MOF/g-C_3N_4 [39], and Nd-ZnO/g-C_3N_4 [40].

Table S1(cf. ESM) further shows the comparative performance of Pr(0.4)g-C_3N_4 relative to some of the photocatalysts which have been commercialized, including TiO_2, ZnO, SnO_2, and WO_3. Despite the relatively high cost of Pr as the dopants, we should note that those commercial catalysts showed very limited activity toward MB removal, even with the use of 2–3 fold dosage or in the solution with a much lower initial MB concentration. Most importantly, as compared with the UV light used for those conventional catalysts, making up only 5% of the sunlight, we utilized visible light, which accounts for approximately 50% of the sunlight spectrum. It will also reduce the operation cost and complexity in a real application. Additionally, the chemical characteristics of Pr as a RE metal are believed to offer Pr(0.4)g-C_3N_4 comparative advantages relative to many of conventional and commercial photocatalysts (such as TiO_2, ZnO, etc.), including enhanced visible light absorption, improved photostability, reduced toxicity, stable oxidation states, and redox property [41−44].

3.2 Operation optimization using Pr(0.4)g-C_3N_4

3.2.1 Effect of catalyst dosage

Figure 8(a) shows a rise in the MB removal by increasing photocatalyst dosage from 0.1 to 0.8 g·L^{-1}. Approximately 59.7%, 74.4%, and 95.6% were removed at the dosages of 0.1, 0.2, and 0.4 g·L^{-1}, respectively. The corresponding pseudo-first-order rate constants (k) were 0.018, 0.028, and 0.108 min^{-1}, respectively. This improved performance with dosage might be ascribed to the increase in the number of exposed surfaces of the Pr(0.4)g-C_3N_4 to the adsorbates, thereby increasing the amount of adsorbed MB (see Fig. 8(a)). Furthermore, the exposure of more active sites might have facilitated the adsorption of light and production of reactive species for the photocatalytic degradation [45]. At a higher dosage (0.8 g·L^{-1}), the total MB removal using Pr(0.4)g-C_3N_4 was reduced to around 89.1% with a k of 0.0420 min^{-1}. This occurred despite an increase in adsorption sites,

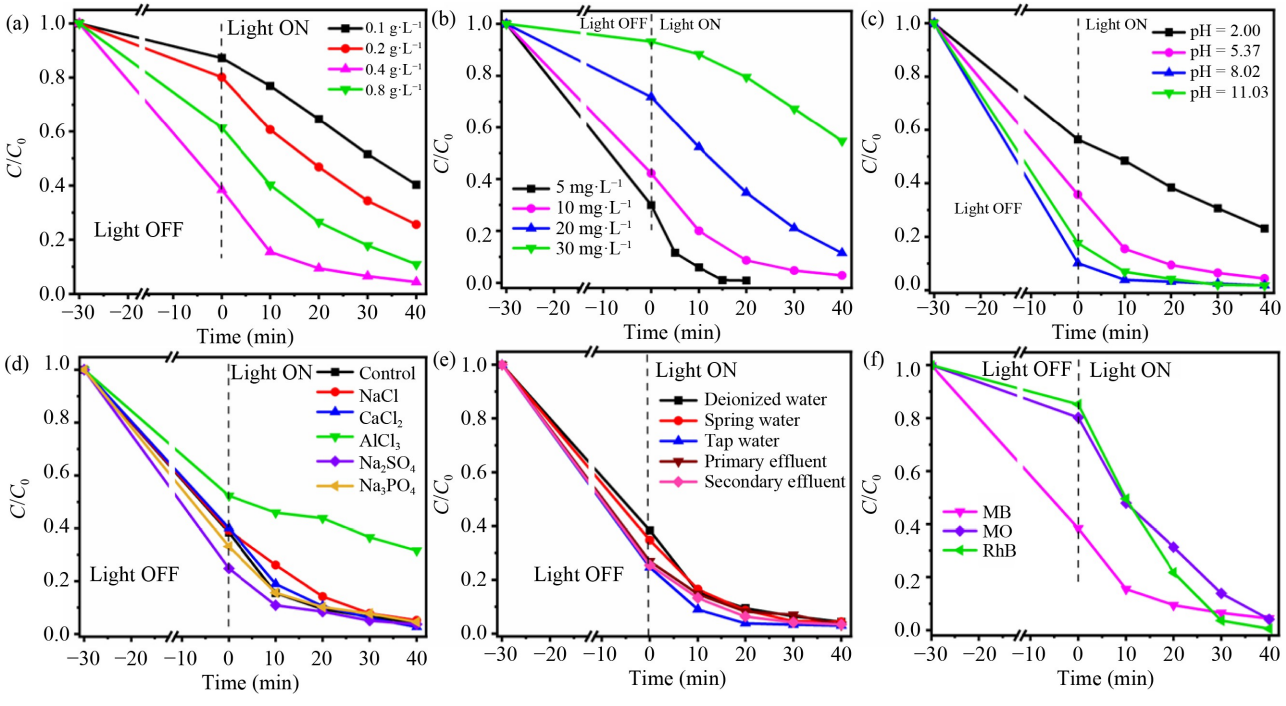

Fig. 8 (a) Effect of dosage (C_i = 10 mg·L^{-1}, catalyst dosage = 0.1–0.8 g·L^{-1}, and pH = 5.37), (b) effect of initial concentration of MB (C_i = 5–30 mg·L^{-1}, catalyst dosage = 0.4 g·L^{-1}, pH = 5.37, and temperature = 25 °C), (c) effect of pH (pH = 2.00–11.03, C_i = 10 mg·L^{-1}, catalyst dosage = 0.4 g·L^{-1}, and temperature = 25 °C), (d) effect of inorganic ions (C_i = 10 mg·L^{-1}, pH = 5.37, catalyst dosage = 0.4 g·L^{-1}, concentration of inorganic ions = 0.2 mol·L^{-1}, and temperature = 25 °C), (e) effect of water matrices, and (f) effect of different dyes using Pr(0.4)g-C_3N_4 (pH_{MO} = 5.67, pH_{MB} = 5.37, pH_{RhB} = 4.00, C_i = 10 mg·L^{-1}, catalyst dosage = 0.4 g·L^{-1}, and temperature = 25 °C).

leading to good adsorption. The reduced performance may be attributed to the increased turbidity of suspension and the agglomeration of catalyst particles, preventing light from reaching the photocatalyst surface, decreasing exposed active sites, and thus reducing the amount of photogenerated charge carriers available for the formation of reactive oxygen species [46].

3.2.2 Effect of initial MB concentration

In Fig. 8(b), Pr(0.4)g-C_3N_4 exhibited a decrease in MB removal efficiency as the initial MB concentrations rose from 5 to 30 mg·L^{-1}. Approximately 99.1% of the MB was removed at 5 mg·L^{-1} MB concentration within 20 min, while only ca. 45.3% efficiency was recorded at an initial concentration of 30 mg·L^{-1}. Accordingly, the rates of k decreased, in the order of 5 mg·L^{-1} (0.182 min^{-1}) > 10 mg·L^{-1} (0.108 min^{-1}) > 20 mg·L^{-1} (0.041 min^{-1}) > 30 mg·L^{-1} (0.012 min^{-1}). This can be associated with the limited adsorptive sites of the photocatalyst available for the increasing amount of MB molecules [47]. Additionally, light penetration was reduced at a high initial concentration of MB, thereby decreasing the amount of visible light reaching the surface of Pr(0.4)g-C_3N_4 and reducing the number of reactive radicals generated for degradation. Meanwhile, a greater amount of MB molecules might occupy the active sites on Pr(0.4)g-C_3N_4 and in turn reduce the generation of reactive species for the photocatalytic reaction.

3.2.3 Effect of initial pH

Given the potential variation of pH in industrial wastewater containing dyes, the effect of pH on the photocatalytic activity of Pr(0.4)g-C_3N_4 was explored in the pH range of 2–11. The degradation efficiency was improved with an increase in the pH value (Fig. 8(c)). MB is a cationic dye in nature, which implies it can be adsorbed onto a negatively charged catalyst surface. The point of zero charge (pzc) of Pr(0.4)g-C_3N_4 was experimentally determined to be 7.8 (Fig. S9, cf. ESM). This infers that at a solution pH < pH_{PZC} of Pr(0.4)g-C_3N_4 (7.8), the surface of the photocatalyst was positively charged and had limited adsorption of the positively charged MB ions. At a solution pH > pH_{PZC} of Pr(0.4)g-C_3N_4 (7.8), it gave rise to a negatively charged surface, which would increase the adsorption of positively charged MB ions through electrostatic attraction. The high adsorption efficiency at pH > 8 in Fig. 8(c) corroborates this. The highest removal efficiency was recorded at pH = 8–11, which may be due to the electrostatic attraction between the negatively charged surface of Pr(0.4)g-C_3N_4 and the cationic MB molecules. However, we noted a relatively high total removal of MB at pH ~5 with a considerable amount of MB adsorbed in the dark. This might be due to the possible complexation between the Pr dopants and the functional groups of dye [15], and electron-donor π–π interaction between the π-electron deficient tri-*s*-triazines of carbon nitride and the aromatic rings of dye. The hydrogen bonding between the hydroxyl groups on Pr(0.4)g-C_3N_4 and the nitrogen atoms of MB molecules would also create attraction [48].

3.2.4 Effect of counter ions

Counter ions, which are commonly found in various water sources, can adversely affect the photocatalytic activity of a photocatalyst through adsorption on the catalyst's active sites or interaction with the target pollutant. Cl^-, SO_4^{2-}, and PO_4^{3-} were selected as counter anions, while Ca^{2+} and Al^{3+} were chosen as counter cations. In Fig. 8(d), the effect of Ca^{2+} was negligible on the adsorptive capacity and photocatalytic performance of Pr(0.4)g-C_3N_4. However, the presence of Al^{3+} largely reduced the total removal % of MB (~70%), including adsorption and photocatalytic degradation (k = 0.012 *vs.* 0.108 min^{-1} for the control), attributable to the electrostatic repulsion between Al^{3+} and the positively charged surface of the photocatalyst which may interfere with the forces of interaction between the MB dye and Pr(0.4)g-C_3N_4, namely, complexation, electron-donor π–π interaction, and hydrogen bonding. On the other side, the counter anions all exhibited an inhibitory effect on the photocatalytic activity of Pr(0.4)g-C_3N_4. The SO_4^{2-} might inhibit the kinetics of the degradation process by reacting with holes or hydroxyl radicals to form less reactive sulfate radicals [49]. The PO_4^{3-} may interact with reactive oxygen species to form weaker radical species, thus slowing down the rate of degradation [50]. The decrease in the degradation rate by Cl^- may be due to its scavenging of photogenerated holes or hydroxyl radicals to generate dichloride anion radicals [49]. Despite some variations in the adsorption and photocatalysis, the overall MB removal by Pr(0.4)g-C_3N_4 was measured to be ca. 95% in the presence of different counter ions (apart from Al^{3+}), thus demonstrating the robustness of Pr(0.4)g-C_3N_4 for potential practical application.

3.2.5 Effect of water matrices

The photocatalytic degradation efficiency of Pr(0.4)g-C_3N_4 was studied in different water matrices, including tap water and spring water, primary and secondary effluents, which were collected at a Perth municipal wastewater treatment plant, in relative to the control (in deionized water) (Fig. 8(e)). We surprisingly found Pr(0.4)g-C_3N_4 showed a slightly improved MB removal performance in all water matrices compared to deionised water, with greater adsorptive capacity along with good photocatalytic activity. Table S2 (cf. ESM) compares the characteristics of different water matrices utilized herein. It is apparent that variations in salinity, conductivity, and

turbidity did not cause significantly detrimental effects on adsorption and photocatalysis in terms of MB removal. As noted previously, it is believed that the pH of water matrix played an important role in determining MB adsorptive removal and photocatalytic reaction. As evidenced in Fig. S9 (cf. ESM), the pzc of Pr(0.4)g-C_3N_4 was experimentally measured to be 7.8, indicating that the catalyst surface was negatively charged and favorable to attract the positively charged MB ions at the pH of the solution > 7.8. As can be seen in Table S2 (cf. ESM), the pH values of spring water, tap water, and effluents are all greater than that of deionized water, contributing to the improved adsorption of MB in the first 30 min in the dark. Especially, in the tap water, which had the highest pH, it had the highest adsorptive removal and photocatalytic reaction rate. As can be seen, Pr(0.4)g-C_3N_4 demonstrated high performance toward MB removal in all water environments (even with elevated salinity, total organic carbon, and turbidity), and thus showed promising potential in practical application.

3.2.6 Effect of different dyes

The universality of Pr(0.4)g-C_3N_4 for removing other types of dyes, including MO and RhB as representative anionic and zwitterionic dyes, was investigated and compared with MB as a representative cationic dye (Fig. 8(f)). The as-prepared Pr(0.4)g-C_3N_4 showed better adsorption and removal rates for cationic MB (k = 0.108 min^{-1}) compared to RhB (k = 0.071 min^{-1}) and MO (k = 0.055 min^{-1}). In Fig. S10 (cf. ESM), the efficiency of Pr(0.4)g-C_3N_4 was significantly boosted compared to g-C_3N_4 for removing MB, MO, and RhB, with rate performance fold estimated at 3.2, 3.8, and 2.9, respectively. On the other side, the adsorptive capability and photocatalytic activity of Pr(0.4)g-C_3N_4 for the removal of MB, MO, and RhB were compared to those of g-C_3N_4, Na(0.4)g-C_3N_4, and Fe(0.4)g-C_3N_4 (Fig. 1(a) and S11 (cf. ESM)). As shown, the Pr(0.4)g-C_3N_4 catalyst exhibited excellent overall removal of MO, RhB, and MB, achieving > 95% within 40 min of visible light illumination, reflecting its robustness in degrading organic dyes regardless of the molecule structure and/or ionic form.

In Fig. 1(a) and Fig. S11 (cf. ESM), we noticed a sharp contrast in the adsorption of MB onto Pr(0.4)g-C_3N_4, Na(0.4)g-C_3N_4, and Fe(0.4)g-C_3N_4. Figure S9 (cf. ESM) shows pH_{pzc} of Pr(0.4)g-C_3N_4, Na(0.4)g-C_3N_4, and Fe(0.4)g-C_3N_4 as 7.8, 9.5, and 9.1, suggesting positively charged surfaces of the catalysts in the solution containing different dyes (initial pH = 4–6). On the one side, the adsorptive removal of cationic MB using Pr(0.4)g-C_3N_4 was most significant, as ~65%, in comparison with 20% and 10% for anionic MO and zwitterionic RhB. As reported in the literature, dye molecules were adsorbed by various mechanisms, such as electrostatic interaction, complexation, π-π stacking, and hydrogen bonding [51]. Considering the catalyst surface charge, dye molecular structure and charge, we believe that the complexation between the RE ions and MB molecules (nitrogen-containing functional groups) and then the formation of complexes [52], appear more prominent than other interactions including the electrostatic repulsion between the positively charged Pr(0.4)g-C_3N_4 and MB. Despite the presence of electrostatic attraction, the adsorptive removal of anionic MO molecules by Pr(0.4)g-C_3N_4 was much lower than that of cationic MB. This might be related to the reduced complexation, which was caused by the coordination orientation and steric hindrance between Pr and MO, and the instability of the formed complexes. It also suggests the significant role of complexation between the RE elements and pollutants governing adsorption.

3.2.7 Reusability and stability

The reusability of Pr(0.4)g-C_3N_4 was tested through five cycles of photocatalytic degradation under similar reaction conditions. Figure 9(a) reveals that appreciable MB removal efficiency was still maintained after five cycles of the test. Figure 9(b) compares the XRD patterns of the fresh and used Pr(0.4)g-C_3N_4. For both samples, two main peaks at 13.1° and 27.3°, ascribed to the in-plane periodic stacking of tri-s-triazine and the interlayer stacking of conjugate aromatic rings in g-C_3N_4, were seen with no significant difference. On the other side, as compared with the FTIR spectrum of the fresh Pr(0.4)g-C_3N_4 (Fig. 9(c)), the used Pr(0.4)g-C_3N_4 exhibited similar characteristic peaks at 810, 1200–1640, and 2971–3390 cm^{-1}. Figure 9(d) shows the microstructure of the used Pr(0.4)g-C_3N_4, largely maintaining nanosheet structure, as observed in the fresh sample (Fig. 4(a)). Figure 9(e) demonstrates the (111), (200), (220), and (311) planes of Pr_6O_{11} [17,28], suggesting the presence of Pr dopants in Pr(0.4)g-C_3N_4 after recycle and reuse. This was further supported by the uniform distribution of those dopants, as can be seen in the EDS mapping analysis (Fig. 9(f)). Therefore, our prepared Pr(0.4)g-C_3N_4 has been proven to maintain its original chemical, crystal, microstructural, and elemental properties after 5 cycles of use. It demonstrated good reusability and stability, as would be required for practical application in wastewater treatment.

3.3 Degradation mechanism

Figure 10(a) explores the roles of active species, including holes (h^+), hydroxyl (•OH), and superoxide ($•O_2^-$), and singlet oxygen ($^1O_2$), in the reaction with the photocatalyst of Pr(0.4)g-C_3N_4 by using different reagents (e.g., Na_2-EDTA, IPA, BQ, and L-Trp.) as scavengers. The residual MB concentration (C/C_0) was

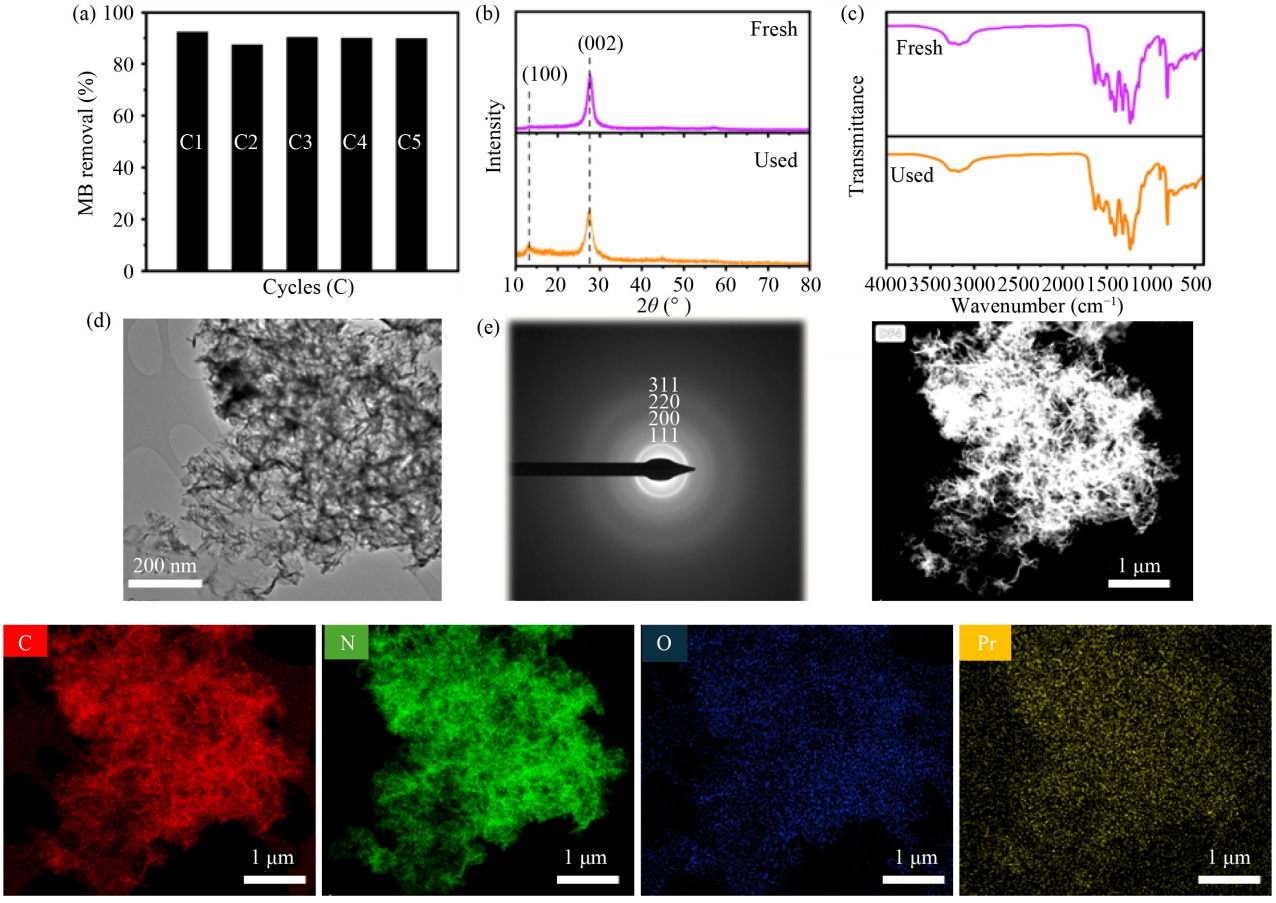

Fig. 9 (a) Photocatalytic degradation test for 5 cycles (reaction conditions: catalyst dosage = 0.4 g·L^{-1}; concentration of MB = 10 mg·L^{-1}; pH = 5.37; temperature = 25 °C); (b) XRD pattern and (c) FTIR spectra of fresh and spent Pr(0.4)g-C_3N_4 after the 5th cycle; (d) TEM image, (e) SAED, and (f) HAADF and EDS mapping of used Pr(0.4)g-C_3N_4.

highest in the presence of L-Trp, suggesting $^1O_2$ as the most critical active species for the photocatalytic degradation of MB in the presence of Pr(0.4)g-C_3N_4. The impact of scavengers in limiting the catalyst performance can be arranged in increasing order of Na_2-EDTA < IPA < BQ < L-Trp. Therefore, the order of increasing significance of active species was determined to be h^+ < •OH < $•O_2^-$ < $^1O_2$. Furthermore, the ESR technique was employed to investigate the active species generated by varying the period of time under visible light illumination.

Figure 10(b) displays the ESR triplet peaks of TEMP-$^1O_2$ adduct with a ratio of 1:1:1. The observed signal in the dark reaction may be ascribed to the chemically adsorbed oxygen on the surface of the photocatalyst [53]. The peak intensity of the TEMP-$^1O_2$ progressively increased, suggesting the continuous generation of $^1O_2$ with reaction time. In Fig. 10(c), no apparent peaks associated with $O_2•^-$ were detected in the dark; however, the DMPO-$O_2•^-$ adducts peaks emerged and became more noticeable on more prolonged exposure of the photocatalyst to visible light. Similarly, the characteristic ESR peaks for •OH were not detected in the dark reaction condition (Fig. 10(d)). Upon illumination and especially after 10 min, the DMPO-•OH adducts with a ratio of 1:2:2:1 were identified, implying the presence of •OH in the photocatalytic reaction. Figure 10(e) shows the ESR peak pattern of TEMPO in the dark. The slight decrease in the peak intensity is associated with the reaction of the photogenerated h^+ to form the TEMPO-h^+ adduct, which has no ESR signal. The marginal attenuation of the h^+ on the peak intensity of TEMPO highlights the auxiliary role in the photocatalytic reaction, which is consistent with the scavenging experiment.

Figure S12(a) (cf. ESM) shows the electronic structure of Pr(0.4)g-C_3N_4, which was established from the Mott-Schottky and UV-Vis DRS analysis; while Fig. S12(b) (cf. ESM) illustrates the possible mechanism for photocatalytic degradation of MB using Pr(0.4)g-C_3N_4, based on the characterization and the radical scavenging results. Upon visible light illumination of Pr(0.4)g-C_3N_4 with energy > E_g, the photogenerated electrons migrated to the CB, leaving holes behind in the VB. Meanwhile, the Pr_6O_{11} was inactive to visible light due to its large band gap (> 3.15 eV); however, it could attract electrons from the CB of Pr(0.4)g-C_3N_4 [17]. Thus, photogenerated electrons migrated to the Pr_6O_{11}, reacting with available dissolved oxygen. The CB electrons of Pr(0.4)g-C_3N_4

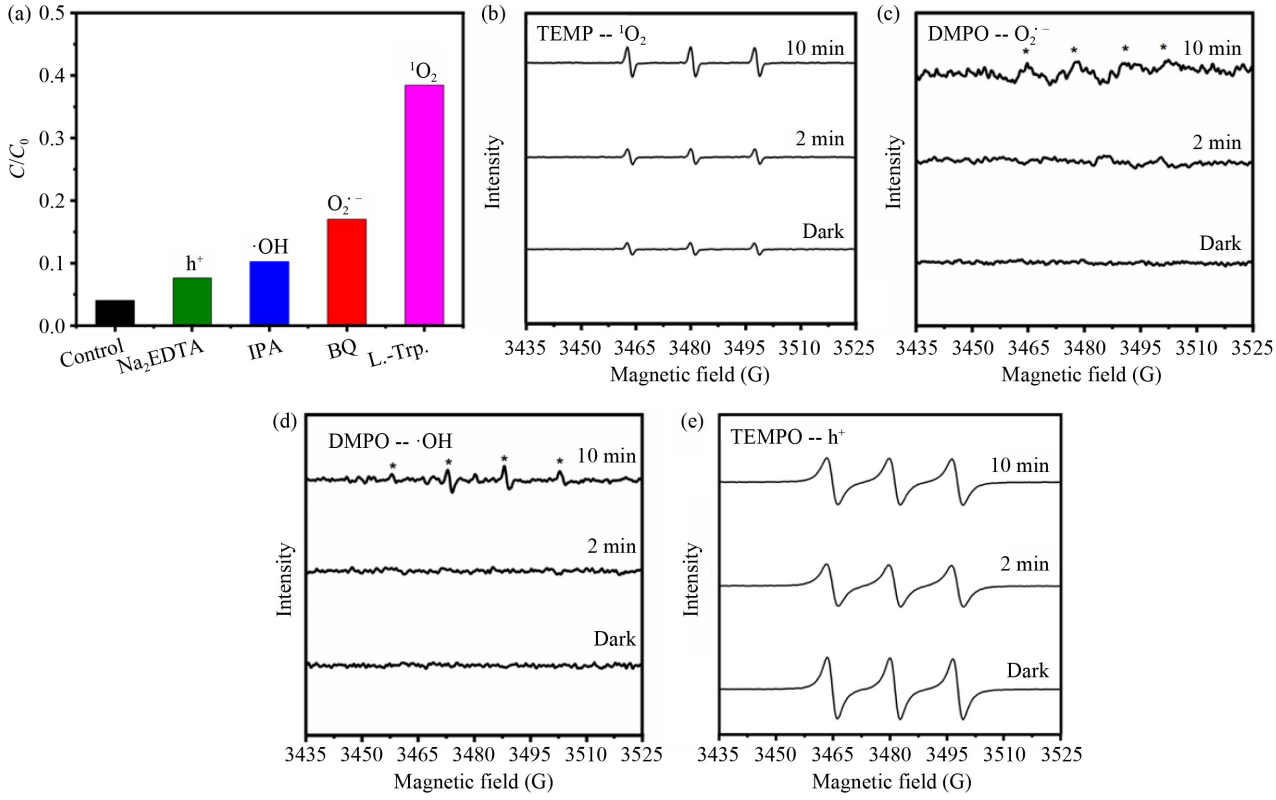

Fig. 10 (a) Effect of radical scavengers on the photocatalytic degradation of MB using Pr(0.4)g-C_3N_4; time-dependent ESR spectra of (b) TEMP-$^1O_2$, (c) DMPO-•O_2^-, (d) DMPO-•OH, and (e) TEMPO-h^+.

(E = –0.59 eV *vs*. NHE) had more negative potential than E^0 (O_2/•O_2^-) = –0.33 eV *vs*. NHE and thus oxidize the dissolved oxygen in the reaction medium to form •O_2^- [54]. Subsequently, the •OH produced from the reaction between the •O_2^- and H_2O degraded the MB molecule. Likewise, •O_2^- can be converted into $^1O_2$ via an oxidative reaction with photogenerated h^+ [55]. The MB molecules were degraded by the $^1O_2$, consistent with results reported in the literature [56]. The dominant role of $^1O_2$ (as seen in Fig. 10(a)) may be attributed to the improved photogenerated electron-hole separation of the photocatalyst with accumulated electrons on its surface for reaction with oxygen under visible light illumination to generate $^1O_2$ for degrading the organic molecules [57]. On the other hand, the photogenerated holes (E = 2.04 eV *vs*. NHE) did not possess the minimum energy required for the oxidation of water to •OH (E = 2.34 eV *vs*. NHE) [54]. Thus, the direct oxidation of water to •OH is not feasible by the as-prepared Pr(0.4)g-C_3N_4. Instead, the photogenerated holes are directly utilized to oxidize the MB molecules. Equations (3–8) show a summary of the possible photocatalytic reactions:

$$\mathrm{Pr(0.4)g-C_3N_4} + h\nu \rightarrow \mathrm{Pr(0.4)g-C_3N_4}(e_{CB}^- + h_{VB}^+) \quad (3)$$

$$\mathrm{Pr(0.4)g-C_3N_4}(e_{CB}^-) + \mathrm{O_2} \rightarrow \mathrm{Pr(0.4)g-C_3N_4} + \bullet\mathrm{O_2^-} \quad (4)$$

$$\bullet\mathrm{O_2^-} + 2\mathrm{H_2O} \rightarrow 2(\bullet\mathrm{OH}) + \mathrm{H_2O_2} \quad (5)$$

$$\bullet\mathrm{O_2^-} + h^+ \rightarrow {}^1\mathrm{O_2} \quad (6)$$

$$\mathrm{Pr(0.4)g-C_3N_4}(h_{VB}^+) \rightarrow \mathrm{Pr(0.4)g-C_3N_4} + h_{VB}^+ \quad (7)$$

$${}^1\mathrm{O_2}/\mathrm{O_2^-}/\bullet\mathrm{OH}/h_{VB}^+ + \mathrm{MB} \rightarrow \text{Degraded products} \quad (8)$$

4 Conclusions

This study systematically examined the characteristics and photocatalytic activity of g-C_3N_4, which was modified by Na (alkali), Fe (transition), and Pr (RE) for the first time. Urea was selected as a suitable and economical precursor for the synthesis of g-C_3N_4. The doped g-C_3N_4 was then prepared by our simple approach, via integration of ion intercalation and thermal treatment, and was expected to improve the photocatalytic activity of g-C_3N_4. Pr(0.4)g-C_3N_4 showed superior photocatalytic activity, with > 95% of total MB, MO, or RhB removal within 40 min of visible light illumination, as compared with Na(0.4)g-C_3N_4 and Fe(0.4)g-C_3N_4. A series of Pr(x)g-C_3N_4 by varying amounts of Pr loading was prepared and then characterized in detail. Our experimental results proved the outstanding photocatalytic activity of Pr(0.4)g-C_3N_4 for organic removal, credited to the enlarged porosity and surface area, improved visible light absorption, enhanced charge carrier density,

promoted charge separation, and reduced charge transfer resistance. Pr(0.4)g-C_3N_4 also demonstrated excellent reusability, retaining a removal efficiency of > 95% after the 5th cycle of reuse, with good chemical and structural stability. The key reactive species involved in the photocatalytic reaction were identified as singlet oxygen radicals.

When compared with other doped g-C_3N_4 photocatalysts in the literature and some commercial catalysts (TiO_2, ZnO, SnO_2, and WO_3), our developed Pr(0.4)g-C_3N_4 showed several advantages, including facile synthesis, high removal, fast degradation, and good reusability. These would endow great potential for commercialization of our catalyst in industrial-scale synthesis and practical application. On the other side, our results highlighted the versatility of our synthesis method for doping of g-C_3N_4 with various species, and we anticipate adopting this approach in the future to prepare photocatalysts applicable in other fields, including renewable energy (batteries), sensors, hydrogen generation, etc.

So far, research efforts have also been reported to explore membrane materials by incorporating catalyst powders for photocatalysis [58,59]. Based on the successful development of the Pr(0.4)g-C_3N_4 powder form herein, our future work will move toward the design of Pr(0.4)g-C_3N_4-based polymer (such as polyvinylidene fluoride) membranes, which is expected to further facilitate the separation of charge carriers, pollutant removal performance and handling for large-scale water treatment, thus potentially reducing the practical operational cost and complexity using our as-prepared catalyst. Moreover, we will exploit different modified g-C_3N_4 using our facile synthetic method for H_2O_2 production by the simultaneous application of piezo-photocatalytic effects to maximize the process efficiency and in turn minimize the cost associated with the dopants.

Competing interests The authors declare that they have no competing interests.

Acknowledgements The authors acknowledge Juita and Malgorzata Kowalczyk for their training and discussion on the analysis. The authors acknowledge the use of equipment and scientific and technical assistance of the Curtin University Electron Microscope Facility and the help from Elaine Miller.

Electronic Supplementary Material Supplementary material is available in the online version of this article at https://doi.org/10.1007/s11705-025-2586-6 and is accessible for authorized users.

Furding Note Open access funding enabled and organized by CAUL and its Member Institutions.

References

1. Zhang X, Yuan X, Jiang L, Zhang J, Yu H, Wang H, Zeng G. Powerful combination of 2D g-C_3N_4 and 2D nanomaterials for photocatalysis: recent advances. Chemical Engineering Journal, 2020, 390: 124475
2. John K I, Ho G, Li D. Recent progresses in synthesis and modification of g-C_3N_4 for improving visible-light-driven photocatalytic degradation of antibiotics. Water Science and Technology, 2024, 89(11): 3047–3078
3. Zhang H, Tang Y, Liu Z, Zhu Z, Tang X, Wang Y. Study on optical properties of alkali metal doped g-C_3N_4 and their photocatalytic activity for reduction of CO_2. Chemical Physics Letters, 2020, 751: 137467
4. Cui W, Chen P, Chen L, Li J, Zhou Y, Dong F. Alkali/alkaline-earth metal intercalated g-C_3N_4 induced charge redistribution and optimized photocatalysis: status and challenges. Journal of Physics: Energy, 2021, 3(3): 032008
5. Zhang J, Hu S, Wang Y. A convenient method to prepare a novel alkali metal sodium doped carbon nitride photocatalyst with a tunable band structure. RSC Advances, 2014, 4(108): 62912–62919
6. Wu S, Yu Y, Qiao K, Meng J, Jiang N, Wang J. A simple synthesis route of sodium-doped g-C_3N_4 nanotubes with enhanced photocatalytic performance. Journal of Photochemistry and Photobiology A Chemistry, 2021, 406: 112999
7. Kalidasan K, Mallapur S, Munirathnam K, Nagarajaiah H, Reddy M B M, Kakarla R R, Raghu A V. Transition metals-doped g-C_3N_4 nanostructures as advanced photocatalysts for energy and environmental applications. Chemosphere, 2024, 352: 141354
8. Gao J, Wang Y, Zhou S, Lin W, Kong Y. A facile one-step synthesis of Fe-doped g-C_3N_4 nanosheets and their improved visible-light photocatalytic performance. ChemCatChem, 2017, 9(9): 1708–1715
9. Ma T, Shen Q, Xue B Z J, Guan R, Liu X, Jia H, Xu B. Facile synthesis of Fe-doped g-C_3N_4 for enhanced visible-light photocatalytic activity. Inorganic Chemistry Communications, 2019, 107: 107451
10. Karimi M A, Iliyat M, Atashkadi M, Ranjbar M, Habibi-Yangjeh A. Microwave-assisted synthesis of the Fe_2O_3/g-C_3N_4 nanocomposites with enhanced photocatalytic activity for degradation of methylene blue. Journal of the Chinese Chemical Society, 2020, 67(11): 2032–2041
11. Wang L, Wang Y, Li X, He T, Wang R, Zhao Y, Song H, Wang H. 3D/2D Fe_2O_3/g-C_3N_4 Z-scheme heterojunction catalysts for fast, effective, and stable photo Fenton degradation of azo dyes. Journal of Environmental Chemical Engineering, 2021, 9(5): 105907

12. Li G, Wang B, Zhang J, Wang R, Liu H. Er-doped g-C_3N_4 for photodegradation of tetracycline and tylosin : high photocatalytic activity and low leaching toxicity. Chemical Engineering Journal, 2020, 391: 123500
13. Li G, Wang R, Wang B, Zhang J. Sm-doped mesoporous g-C_3N_4 as efficient catalyst for degradation of tylosin: influencing factors and toxicity assessment. Applied Surface Science, 2020, 517: 146212
14. Tuna Ö, Simsek E B. Synergic contribution of intercalation and electronic modification of g-C_3N_4 for an efficient visible-light-driven catalyst for tetracycline degradation. Journal of Environmental Chemical Engineering, 2020, 8(5): 104445
15. Kalpakli Y. The effect of in-situ Pr_6O_{11} phase formation on photocatalytic performance: mono azo dye degradation. Inorganic Chemistry Communications, 2024, 159: 111788
16. Swetha S, Abdel-Maksoud M A, Okla M K, Janani B, Dawoud T M, El-Tayeb M A, Khan S S. Triple-mechanism driven Fe-doped *n-n* hetero-architecture of Pr_6O_{11}-MoO_3 decorated g-C_3N_4 for doxycycline degradation and bacterial photoinactivation. Chemical Engineering Journal, 2023, 461: 141806
17. Shende A G, Ghugal S G, Vidyasagar D, Kokane S B, Jagannath, Umare S S, Sasikala R. Solvent free solid-state synthesis of Pr_6O_{11}/g-C_3N_4 visible light active photocatalyst for degradation of AV7 dye. Materials Research Bulletin, 2018, 107: 154–163
18. Jiang J, Cao S, Hu C, Chen C. A comparison study of alkali metal-doped g-C_3N_4 for visible-light photocatalytic hydrogen evolution. Chinese Journal of Catalysis, 2017, 38(12): 1981–1989
19. Yan W, Yan L, Jing C. Impact of doped metals on urea-derived g-C_3N_4 for photocatalytic degradation of antibiotics: structure, photoactivity, and degradation mechanisms. Applied Catalysis B: Environmental, 2019, 244: 475–485
20. Dong S, Lian X, Chen S, Li H, Liu E, Xu K. Kinetic analysis and mechanism study on the photocatalytic degradation of 2,4-dinitrophenylhydrazine over surface plasmonic Ag/Cu/TiO_2 composite. Reaction Kinetics, Mechanisms, and Catalysis, 2021, 134(1): 485–499
21. Bui T S, Bansal P, Lee B K, Mahvelati-Shamsabadi T, Soltani T. Facile fabrication of novel Ba-doped g-C_3N_4 photocatalyst with remarkably enhanced photocatalytic activity towards tetracycline elimination under visible-light irradiation. Applied Surface Science, 2020, 506: 144184
22. Tonda S, Kumar S, Kandula S, Shanker V. Fe-doped and -mediated graphitic carbon nitride nanosheets for enhanced photocatalytic performance under natural sunlight. Journal of Materials Chemistry A: Materials for Energy and Sustainability, 2014, 2(19): 6772–6780
23. Wang B, Liu X, Dai S, Lu H. α-Fe_2O_3 nanoparticles/porous g-C_3N_4 hybrids synthesized by calcinations of Fe-based MOF/melamine mixtures for boosting visible-light photocatalytic tetracycline degradation. ChemistrySelect, 2020, 5(11): 3303–3311
24. Chi X, Liu F, Gao Y, Song J, Guan R, Yuan H. An efficient B/Na co-doped porous g-C_3N_4 nanosheets photocatalyst with enhanced photocatalytic hydrogen evolution and degradation of tetracycline under visible light. Applied Surface Science, 2022, 576: 151837
25. Wu Y, Yang D, Xu W, Song R, Li M, Wang Y, Zhou B, Wu N, Zhong W, Cai H, et al. Tunable water-soluble carbon nitride by alkali-metal cations modification: enhanced ROS-evolving and adsorption band for photodynamic therapy. Applied Catalysis B: Environmental, 2020, 269: 118848
26. Ansari H M, Wang W, Lei L, Bao K, Chang X, Raza A, Chen Y, Mehboob A, Zhong Q, Srivastava A, et al. Gas bubbling exfoliation strategy towards 3D g-C_3N_4 hierarchical architecture for superior photocatalytic H_2 evolution. Journal of Alloys and Compounds, 2022, 919: 165794
27. Song X, Tao H, Chen L, Sun Y. Synthesis of Fe/g-C_3N_4 composites with improved visible light photocatalytic activity. Materials Letters, 2014, 116: 265–267
28. Dodd A. Synthesis of praseodymium hydroxide ($Pr(OH)_3$) and praseodymium oxide (Pr_6O_{11}) nanorods via room temperature aging. Journal of Colloid and Interface Science, 2012, 392(1): 137–140
29. Nazir R, Fageria P, Basu M, Gangopadhyay S, Pande S. Decoration of Pd and Pt nanoparticles on a carbon nitride (C_3N_4) surface for nitro-compounds reduction and hydrogen evolution reaction. New Journal of Chemistry, 2017, 41(18): 9658–9667
30. Hassan M S, Akhtar M S, Shim K B, Yang O B. Morphological and electrochemical properties of crystalline praseodymium oxide nanorods. Nanoscale Research Letters, 2010, 5(4): 735–740
31. Iqbal S, Liu J, Ma H, Liu W, Zuo S, Yu Y, Khan A. Development of TiO_2 decorated Fe_2O_3QDs/g-C_3N_4 ternary Z-scheme photocatalyst involving the investigation of phase analysis via strain mapping and its photocatalytic performance under visible light illumination. Research on Chemical Intermediates, 2023, 49(8): 3327–3362
32. Gao Z, Chen Z, Zhan X, Zhou L, Xie Y, Yang X, Tian J, Zhang G, Sun S, Tong X. Pt nanoparticles supported on iron and nitrogen-doped holey graphene for boosting ORR performance. ACS Applied Nano Materials, 2023, 6(12): 10521–10530
33. Kumar A, Ravina, Anu, Kumar V, Deopa N, Punia R, Rao A S. Epoxy free LED devices: physical and optical examination of praseodymium doped borate glasses for enhanced performance. Materials Letters: X, 2023, 19: 100210
34. Wei S, Li W, Ma Z, Deng X, Li Y, Wang X. Novel bismuth nanoflowers encapsulated in N-doped carbon frameworks as superb composite anodes for high-performance sodium-ion batteries. Small, 2023, 19(46): 2304265
35. Shu Z, Wang Y, Wang W, Zhou J, Li T, Liu X, Tan Y, Zhao Z. A green one-pot approach for mesoporous g-C_3N_4 nanosheets with *in situ* sodium doping for enhanced photocatalytic hydrogen evolution. International Journal of Hydrogen Energy, 2019, 44(2): 748–756
36. Lv S W, Zheng Q, Ye L, Li C Y, Liu J M, Cong Y, Wang S. The elaborately-designed Z-scheme Fe-g-C_3N_4/α-Fe_2O_3 photocatalytic platform equipping with active N-Fe-O bridges for enhanced synergistic removal of tetracycline and Cr(VI) via photoinduced electron transfer process. Chemical Engineering Journal, 2023, 455: 140940
37. Xu F, Chai B, Liu Y, Liu Y, Fan G, Song G. Superior photo-Fenton activity toward tetracycline degradation by 2D α-Fe_2O_3 anchored on 2D g-C_3N_4: S-scheme heterojunction mechanism and accelerated Fe^{3+}/Fe^{2+} cycle. Colloids and Surfaces A:

Physicochemical and Engineering Aspects, 2022, 652: 129854
38. Gindose T G, Atisme T B, Hailegebreal T D, Zereffa E A. ZnO modified g-C_3N_4-MnO_2 composite for photodegradation of methylene blue. ChemistrySelect, 2025, 10(1): e202403418
39. Durmus Z, Köferstein R, Lindenberg T, Lehmann F, Hinderberger D, Maijenburg A W. Preparation and characterization of Ce-MOF/g-C_3N_4 composites and evaluation of their photocatalytic performance. Ceramics International, 2023, 49(14): 24428–24441
40. Tian M, Zhang G, Zhao X, Yan Y, Zhao J, Bai H, Jiang J. Construction of rare-metal neodymium-doped ZnO and g-C_3N_4 Z-type heterostructures enhance the photocatalytic efficiency of methylene blue removal. Diamond and Related Materials, 2023, 140: 110493
41. Spadavecchia F, Cappelletti G, Ardizzone S, Ceotto M, Azzola M S, Presti L L, Cerrato G, Falciola L. Role of Pr on the semiconductor properties of nanotitania: an experimental and first-principles investigation. Journal of Physical Chemistry C, 2012, 116(43): 23083–23093
42. Xiao J, Ge S, Jiang Z, Liu J, Yuan D, Liang C, Xu M, Li S, Xu H, Wang X, et al. A study on the high mobility and improved reliability of Pr-doped indium zinc oxide thin film transistors. Semiconductor Science and Technology, 2024, 39(11): 115024
43. Leite C, Russo T, Polese G, Soares A, Pretti C, Pereira E, Freitas R. Effects of the interaction of salinity and rare earth elements on the health of nytilus galloprovincialis: the case of praseodymium and europium. Journal of Xenobiotics, 2024, 14(4): 2015–2038
44. Veiga E L S, Fortuño-Morte M, Beltrán-Mir H, Cordoncillo E. Effect of the oxidation states on the electrical properties of Fe-doped $Pr_2Zr_2O_7$ pyrochlore. Journal of Materials Research and Technology, 2022, 16: 201–215
45. Moradi S, Isari A A, Hayati F, Rezaei Kalantary R, Kakavandi B. Co-implanting of TiO_2 and liquid-phase-delaminated g-C_3N_4 on multi-functional graphene nanobridges for enhancing photocatalytic degradation of acetaminophen. Chemical Engineering Journal, 2021, 414: 128618
46. Liu H, Huo W, Zhang T C, Ouyang L, Yuan S. Photocatalytic removal of tetracycline by a Z-scheme heterojunction of bismuth oxyiodide/exfoliated g-C_3N_4: performance, mechanism, and degradation pathway. Materials Today: Chemistry, 2022, 23: 100729
47. Tahir S, Zahid M, Hanif M A, Bhatti I A, Naqvi S A R, Bhatti H N, Jilani A, Alshareef S A, El-Sharnouby M, Shahid I. The synergistic effect of g-C_3N_4/GO/$CuFe_2O_4$ for efficient sunlight-driven photocatalytic degradation of methylene blue. International Journal of Environmental Science and Technology, 2025, 22(6): 4829–4846
48. Wei T, Fu Z, Meng Y, Li C, Yin F, Wang X, Zhang C, Guo L, Sun S. Photocatalytic degradation of methylene blue over MIL-100(Fe)/Go composites: a performance and kinetic study. International Journal of Loal Science & Technology, 2024, 11: 42
49. Kumar A, Sharma K, Thakur M, Pathania D, Sharma A. Fabrication of high visible light active $LaFeO_3$/Cl-g-C_3N_4/RGO heterojunction for solar assisted photo-degradation of aceclofenac. Journal of Environmental Chemical Engineering, 2022, 10(4): 108098
50. Balakrishnan A, Vijaya Suryaa K, Chinthala M, Kumar A. Mechanistic insights of PO_4^{3-} functionalized carbon nitride homojunction hydrogels in photocatalytic-self-Fenton-peroxy-monosulfate system for tetracycline degradation. Journal of Colloid and Interface Science, 2024, 669: 366–382
51. Salahshoori I, Wang Q, Nobre M A L, Mohammadi A H, Dawi E A, Khonakdar H A. Molecular simulation-based insights into dye pollutant adsorption: a perspective review. Advances in Colloid and Interface Science, 2024, 333: 103281
52. Bellardita M, Di Paola A, Palmisano L, Parrino F, Buscarino G, Amadelli R. Preparation and photoactivity of samarium loaded anatase, brookite, and rutile catalysts. Applied Catalysis B: Environmental, 2011, 104(3): 291–299
53. Zhao G, Ding J, Zhou F, Chen X, Wei L, Gao Q, Wang K, Zhao Q. Construction of a visible-light-driven magnetic dual Z-scheme $BiVO_4$/g-C_3N_4/$NiFe_2O_4$ photocatalyst for effective removal of ofloxacin: mechanisms and degradation pathway. Chemical Engineering Journal, 2021, 405: 126704
54. Jiao J, Wang Z, Wang J, Yao T, Chen Z, Chen C, Sun L, Zhao X, Fan W. g-C_3N_4-based homojunction induced by Ag and P selective doping for improved photocatalytic H_2 evolution coupled with tetracycline degradation: type-II versus S-scheme mechanism. Applied Surface Science, 2023, 639: 158260
55. He D, Yang H, Jin D, Qu J, Yuan X, Zhang Y, Huo M, Peijnenburg W J G M. Rapid water purification using modified graphitic carbon nitride and visible light. Applied Catalysis B: Environmental, 2021, 285: 119864
56. Cui R, Jin D, Jiao G, Liu Z, Ma J, Sun R. Cuprous oxide/copper oxide interpenetrated into ordered mesoporous cellulose-based carbon aerogels for efficient photocatalytic degradation of methylene blue. Frontiers of Chemical Science and Engineering, 2023, 17(7): 918–929
57. Yang Y, Bian Z. Oxygen doping through oxidation causes the main active substance in g-C_3N_4 photocatalysis to change from holes to singlet oxygen. Science of the Total Environment, 2021, 753: 141908
58. Lv H, Liu Y, Zhou J, Bai Y, Shi H, Yue B, Shen S, Yu D G. Efficient piezophotocatalysis of ZnO@PVDF coaxial nanofibers modified with $BiVO_4$ and Ag for the simultaneous generation of H_2O_2 and removal of pefloxacin and Cr(VI) in water. Chemical Engineering Journal, 2024, 484(15): 149514
59. Lv H, Wang P, Lv Y, Dong L, Li L, Xu M, Fu L, Yue B, Yu D. Piezo-photocatalytic degradation of ciprofloxacin based on flexible $BiVO_4$ PVDF nanofibers membrane. Catalysts, 2025, 15(2): 163